CASE 1: CUBIC AND EASM MODELLING OF SYNTHETIC JETS

A. K. Preece[1], P. G. Tucker[2], and Y. Liu[1]

[1] *Fluid Dynamics Research Centre, University of Warwick, Coventry, United Kingdom, CV4 7AL*
[2] *Civil and Computational Engineering Centre, University of Wales, Swansea, United Kingdom, SA2 8PP*

Solution Methodology

Computations were carried out using a modified version of the NEAT finite volume code [1]. The convection terms are discretized using the essentially second order central difference based CONDIF [2] scheme. For the diffusion terms, central differences are used. To integrate the equations through time, the Crank-Nicolson scheme is used. Compatible with our future intention to model the jet with LES staggered grids are used.

To provide a pressure field the SIMPLE algorithm [3] was used. For Unsteady Reynolds Averaged Navier-Stokes (URANS) solutions, the use of various solution adaptive time step methods is also being explored.

Model Description

Three URANS turbulence models were used in these simulations, low Reynolds number k-ϵ [4], non-linear k-ϵ (cubic) [5] and Explicit Algebraic Stress Model (EASM) [6]. The implementation of these models is described in [7].

Implementation and Case Specific Details

An unsteady boundary condition was applied at the jet inlet and varied with time as shown in Eqn (1) below.

$$U(t) = Asin(2\pi ft) \tag{1}$$

Where U is the instantaneous jet amplitude (ms^{-1}), A is the maximum jet amplitude of 30ms^{-1}, f is the frequency of 444.7Hz and t is the present time(sec).

The velocity profile of this jet initially set as a top-hat profile but it was seen that applying a seventh power profile improved the accuracy by more correctly modelling the shear layers induced by the walls. Since the fluid density is assumed constant, an unsteady boundary condition was also set across the entire top face of the domain. To improve numerical stability, the side walls were set as solid boundaries. This is shown in Figure 1

An unsteady k and ϵ boundary condition was also set at the inlet. The turbulence intensity was assumed to be 10% (and isotropic) and the length scale, L, was taken as the width of the jet (1.27mm). However, on the suction stroke of the jet cycle, k and ϵ were set to zero in order to simulate no turbulent energy being input into the domain. This is shown by Eqn (2) and (3)

$$k = max[\frac{3}{2}(0.1U(t))^2, 0] \tag{2}$$

$$\epsilon = max[C^{3/4}\frac{k^{3/2}}{l}, 0] \tag{3}$$

where C=0.09 and l=0.07L

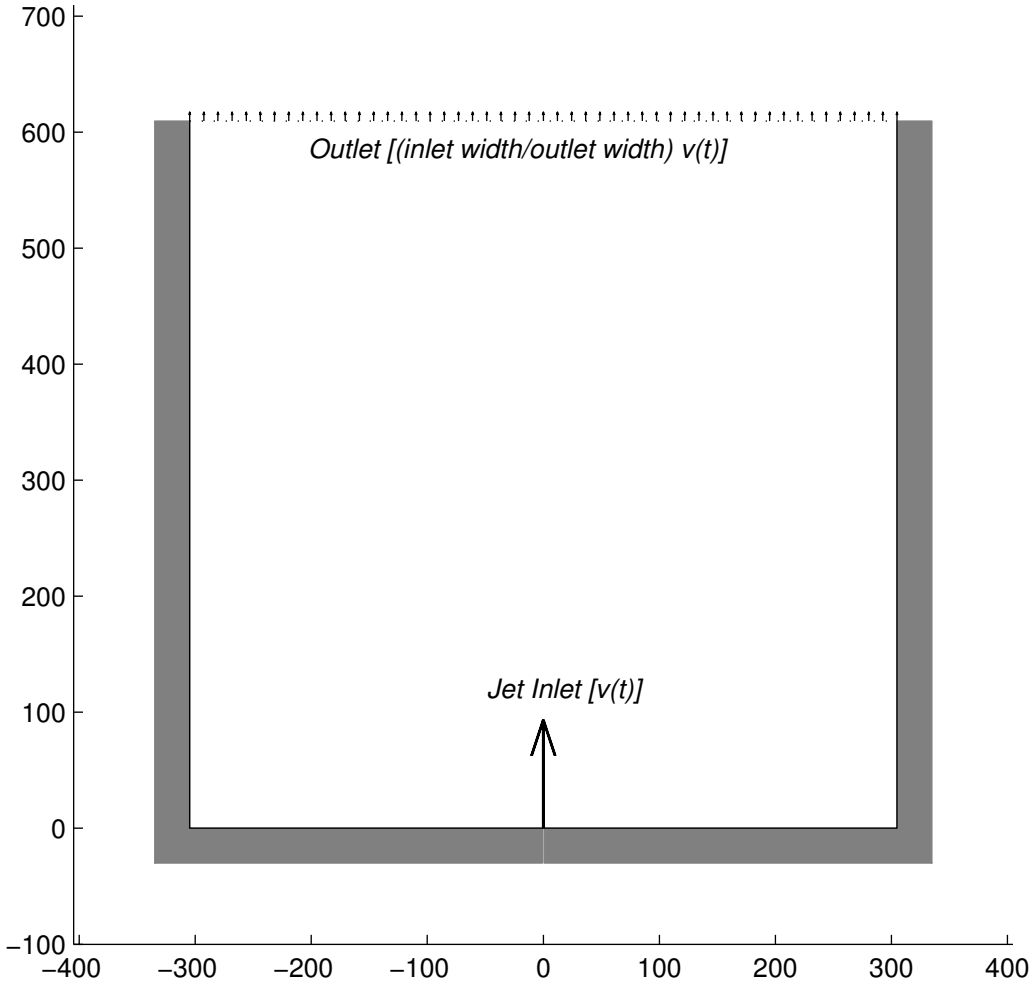

Figure 1: The boundary conditions.

The timestep was chosen to correspond to a tenth of a single degree of the cycle corresponding to 6.25×10^{-7}s. This allowed the phase average to be taken at a discrete number of timesteps rather than having to resort to interpolation between timesteps.

The grid used was of non-uniform rectangular type with 99 grid nodes in the x direction across the jet and 49 nodes in the streamwise y direction. The geometric grid expansion factor was typically about 1.15. The grid is shown in Figure 2. Although quite coarse, this grid allowed reasonably quick simulations to be run. However a finer grid is to be investigated in the future.

Four iterations per timestep were found necessary for convergence. The maximum Courant number is 1.1 (that is where the grid spacing is smallest and velocity highest) but the average Courant number is well below unity. Initial non-cyclic data is discarded. Typically, the flow reached a cyclic state within about 15-20^o

The simulations were run in sequential mode on a SUNFIRE 6800 machine with 24 individual 950MHz processors and 12GB of working memory. This resulted in run times of roughly 60 seconds/timestep for the standard k-e model and 75 seconds/timestep for the cubic and EASM models.

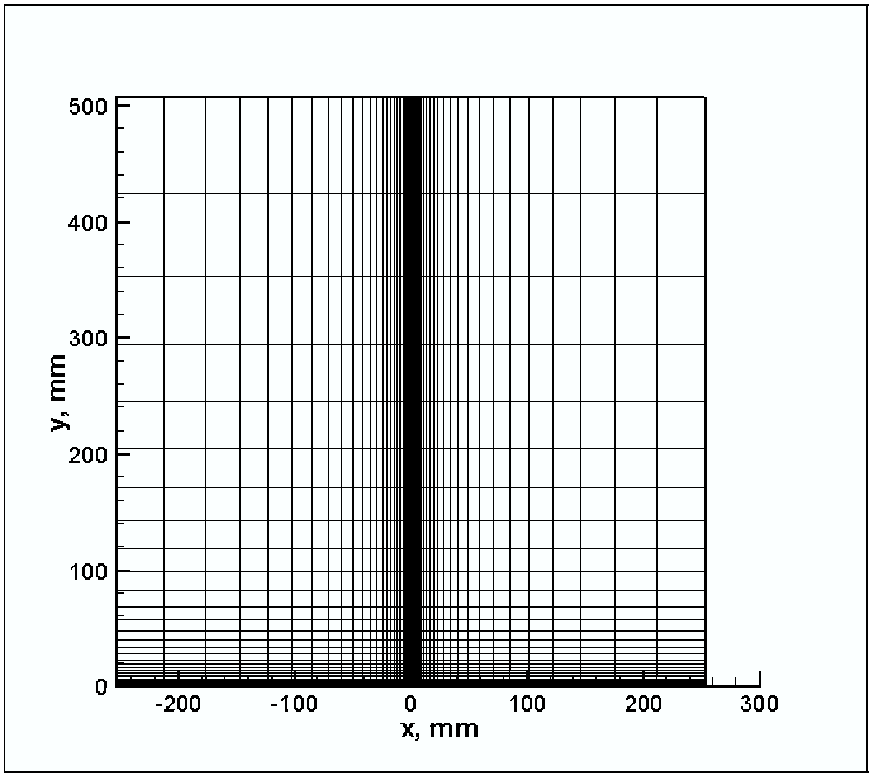

Figure 2: The grid structure used.

References

[1] Tucker, P. G. "Computation of Unsteady Internal Flows,", Kluwer Academic Publishers, pp. 321–331, 2001.

[2] Runchal, A. K. "CONDIF: A modified central-difference scheme for convective flows," *Int. J. Numer. Meth. in Engrg*, Vol. 24, pp. 1593–1608, 1987.

[3] Patankar, S. V. and Spalding D. B. "A calculation procedure for heat mass and momentum transfer in three-dimensional parabolic flows," *Int. J. Heat and Mass Transfer*, Vol. 15, pp. 1787–1806, 1972.

[4] Launder, B. E. and Sharma, B. I. "Application of the energy-dissipation model of turbulence to the calculation of flow near a spinning disc," *Letters in Heat and Mass Transfer*, Vol. 1, pp. 131–136, 1974.

[5] Craft, T. J. and Launder, B.E. "Development and application of a cubic eddy-viscosity model of turbulence," *Int. J. of Heat & Fluid Flow*, Vol. 17, pp. 108–115, 1996.

[6] Gatski, T. B. and Speziale, C. G. "On Explicit Algebraic Stress Models (EASM) for complex turbulent flows," *J. Fluid Mech.*, Vol. 254, pp. 59–78, 1993.

[7] Liu, Y. "Numerical Simulations of Unsteady Complex Geometry Flows," *University of Warwick*, 2004.

CASE 1: NUMERICAL SIMULATION OF A SYNTHETIC JET INTO QUIESCENT AIR USING A STRUCTURED AND AN UNSTRUCTURED GRID FLOW SOLVER

L. Huang, H. Chen, V. Katam, V. Parimi, R. P. LeBeau, and P .G. Huang

Department of Mechanical Engineering, University of Kentucky, Lexington, KY 40506-0108

Introduction

Active flow control technologies is growing area of aerodynamic research in the early 21st century. The goal is to prevent boundary layer separation and as such it is often applied to designs of high-lift airfoils. Forced oscillations superimposed on a mean flow which is on the verge of separation point is an effective means to delay boundary-layer separation, such as blowing or suction techniques. However, the progress in active flow control technologies has often been paced by the development of actuator capabilities. A popular current actuator is the synthetic jet, which has demonstrated capabilities regarding separation control and thrust vectoring.

Our approach to this problem has been to employ two different computational fluid dynamics (CFD) codes—a two-dimensional structured grid solver and a three-dimensional unstructured grid solver. Both codes are in-house codes in use at the University of Kentucky. The structured code, GHOST, uses overlapping Chimera-style grids to model more complicated flows and geometries—the advantages and disadvantages of this type of approach are well-established, although with proper diligence excellent results can be obtained using these methods. However, the continual advances in both computational fluid dynamics (CFD) algorithms and computer technologies have made unstructured grids more attractive with their ability to smoothly conform to varying flow conditions and complicated boundaries with a single grid. Remaining challenges for this type of approach including grid generation for a computational domain with complex geometries, well-balanced grid decomposition on distributed system, and efficient parallel performance. For the three-dimensional simulation of this case, we use a three-dimensional unstructured grid code called UNCLE. While one is structured and one is unstructured, GHOST and UNCLE share some common numerical techniques and as such are quite complementary

Solution Methodology

The two-dimensional simulations presented were computed with GHOST. GHOST is an in-house CFD code developed at University of Kentucky by P. G. Huang. The code is based on a finite volume structured formulation with chimera overset grids. The QUICK and TVD schemes are applied to discretize the convective terms in the momentum and turbulence equations, respectively; the central difference scheme is used for the diffusive terms and the second order upwind time discretization is employed for the temporal terms. This code has been tested extensively and is routinely used for turbulence model validation [1,2,3] and flow control studies [4,5,6]. The turbulence model used in the present computation is Menter's SST two equation model [7], which provides excellent predictive capability for flows with separation [8]. The multi-block and chimera features of the code allow the use of fine gird patches near the jet entrance and in regions of highly active flow. The code also employs MPI parallelization to allow different computational zones to be solved on different processors.

The unstructured grid code is UNCLE. UNCLE is a 2D/3D finite volume unstructured unsteady incompressible Navier-Stokes solver. UNCLE employs a pressure-based SIMPLE

algorithm with second order accuracy in both time and space. A second order upwind scheme is used for computing advection terms. Non-staggered grids with the Rhie and Chow momentum interpolation method [9] are employed to avoid checkerboard solutions. In order to take care of turbulence flow in most realistic cases, F. R. Menter's shear-stress transport (SST) turbulence model [7] is implemented. It is designed to study the challenges of using unstructured grid codes on high-performance parallel computers to simulate realistic cases. To increase flexibility in complex geometries, UNCLE may use a variety of grid types, such as triangles, quadrilateral, tetrahedron and hexahedra meshes. In order to achieve good load balance for parallel computing, METIS [10] is used to partition the grid. Generally, there are two different partitioning approaches – vertex based and element based partitioning for mesh-partitioning as shown in Fig. 1(a) and (b) respectively. For vertex-based partitioning, the boundary elements are doubled and the vertices at the boundary are overlapped. Since the control volumes at boundary are not partitioned, only communication of boundary nodal properties is required. For element-based partitioning, the boundary vertices are doubled. Because the control volumes at the boundary are split, all nodal points surround a boundary vertex are needed to interpolate the properties of the boundary vertices. Communication of boundary nodal properties in element based partitioning is heavier than vertex-based partitioning. On the other hand, vertex-based partitioning has to handle doubled elements at the boundary, it still costs computational time. For the purpose of direct use the information from METIS, element based partitioning is used for pre-processing code of UNCLE.

Both UNCLE and GHOST are designed to run on multiple platforms, notably in this commodity PC clusters on which the bulk of the simulations were performed.

Model Description

The turbulence model used in the present computation is Menter's SST two equation model [7], which provides excellent predictive capability for flows with separation [8], among other challenging flow types. UNCLE likewise employs the M-SST two-equation turbulence model, but has not undergone the extensive "burn-in" that GHOST has received.

Implementation and Case Specific Details

For the current 2-D computations, we use the 2-D grid (structure 2D grid #1 and structure 2D grid #2) provided by the workshop website, in combination with two timesteps (T1=0.003 and T2=0.009), generating 4 sets of results. The following convention is used to name the data files:

G1T1: structure 2D grid #1, and time step T1=0.003.
G1T2: structure 2D grid #1, and time step T1=0.009.
G2T1: structure 2D grid #2, and time step T1=0.003.
G2T2: structure 2D grid #2, and time step T1=0.009.

The non-dimensional time period for one cycle is: $\overline{T} = 52.488$.
The value being chosen to non-dimensionlize the velocity is: $V = 30m/s$.
The Reynolds number is Re=2453.72.

The left hand side boundary of zone 1,2,3,4 (workshop provided grid, moving diaphragm) are given by oscillatory non-dimensional velocity boundary condition. The oscillation is defined by the displacement history at the center of the diaphragm from the PIV experiment provided on the cfdval2004 website translate into the velocity history at the center of the diaphragm. The time-

dependent velocity at the center of the diaphragm can be approximated by curve-fitting method, and its mathematical formulation is described as:
:

$$\frac{v}{V_\infty} = a + b \cdot \cos(c \cdot t + d), \text{ for} \qquad (2)$$

a = - 0.0044205499
b = 0.026689782
c = 0.119707081
d = - 4.0776928

where a, b, c, and d are dimensionless parameters and t is dimensionless time. The u-t plot is shown in Fig. 3. For the top of box, the outflow boundary condition is chosen to satisfy the continuity equation. For the rest of the boundary, the no-slip condition is imposed as a wall boundary condition.

In the unstructured simulations, the slot width, 0.05 inches, is chosen to be the reference length. Air density at sea level set as 1.185kg/m^3, viscosity is 18.4e-6kg/m-s, and the reference velocity is the maximum velocity at the slot exit which is approximately 30m/s. As with the GHOST simulations, the Reynolds number for this case is 2453.7. The single timestep used in these simulations is 0.02 seconds, so the timesteps per cycle is 2624.

An unstructured grid is generated to fulfill the grid format of UNCLE by using GAMBIT. The total grid points are 0.26 million points and the cell are 1.4 million. For this grid, y^+ approximately equals 5 on the wall surface. The geometry of the grid is exactly the same as provided by the cfdval2004 website. Figure 2 (a) and (b) show the global outline and the zoom-in picture of the actuator, respectively.

As with the 2D simulations, a periodic velocity boundary condition replaced the moving boundary condition for the diaphragm. The non-dimensional period T can be calculated by:

$$1/T = f^* = f * \ell / u \qquad (3)$$

where f^* is non-dimensional frequency, frequency f =444.7Hz, reference length ℓ =0.05 in, and reference velocity u =30 m/s. As a result of equation 3, the non-dimensional period T is again 52.48. The diaphragm boundary is approached in the same fashion as the 2D simulation (Eqn 2), as are the other boundary conditions.

Reference

1. Y. B. Suzen, P. G. Huang, "Numerical Simulation of Wake Passing on Turbine Cascades", AIAA-2003-1256, 41st Aerospace Sciences Meeting and Exhibit, Jan. 2003
2. Y. B. Suzen, P.G. Huang, R. J. Volino, T. C. Corke, F. O. Thomas, J. Huang, J. P. Lake and P. I. King, “A Comprehensive CFD Study of Transitional Flows In Low-Pressure Turbines Under a Wide Range of Operation Conditions”, 33rd AIAA Fluid Dynamic Conference, AIAA 2003-3591, June 2003
3. Y. B. Suzen and P. G. Huang, “Predictions of Separated and Transitional Boundary Layers Under Low-Pressure Turbine Airfoil Conditions Using an Intermittency Transport Equation”, Journal of Turbomachinery, Vol. 125, No.3, July 2003, pp. 455-464
4. Munday, D., Jacob, J.D., Hauser, T., and Huang, P.G., “Experimental and Numerical Investigation of Aerodynamic Flow Control Using Oscillating Adaptive Surfaces,” AIAA 2001-2837, June 2002.

5. L. Huang, P.G. Huang, R.P. LeBeau and Th. Hauser, "Numerical Study of Blowing and Suction Control Mechanism on NACA0012 Airfoil", *Journal of Aircraft*, (accepted for publication October, 2003).
6. L. Huang, G. Huang, R. LeBeau, Th. Hauser, "Optimization of Blowing and Suction Cotrol on NACA0012 Airfoil Using Genetic Algorithm", AIAA 2004-0225 42nd Aerospace Sciences Meeting and Exhibit, Jan. 2004
7. F. R. Menter, "Two-Equation Eddy-Viscosity Turbulence Models For Engineering Applications", AIAA Journal, Vol. 32, No. 8, Aug. 1994, pp. 1598-1605
8. Bardina, J. E., P. G. Huang and T. J. Coakley, "Turbulence Modeling Validation, Testing and Development", NASA TM-110446, April 1997
9. Rhie, C. M. and Chow, W. L., "Numerical study of the turbulent flow past an airfoil with tailing edge separation," *J. AIAA*, 21, pp. 1525-1532.
10. Karypis, G. and Kumar, V., "A software package for partitioning unstructured graphs, partitioning meshes, and computing fill-reducing orderings of sparse matrices version 4.0," http://www.cs.umn.edu/~karypis, 1998.

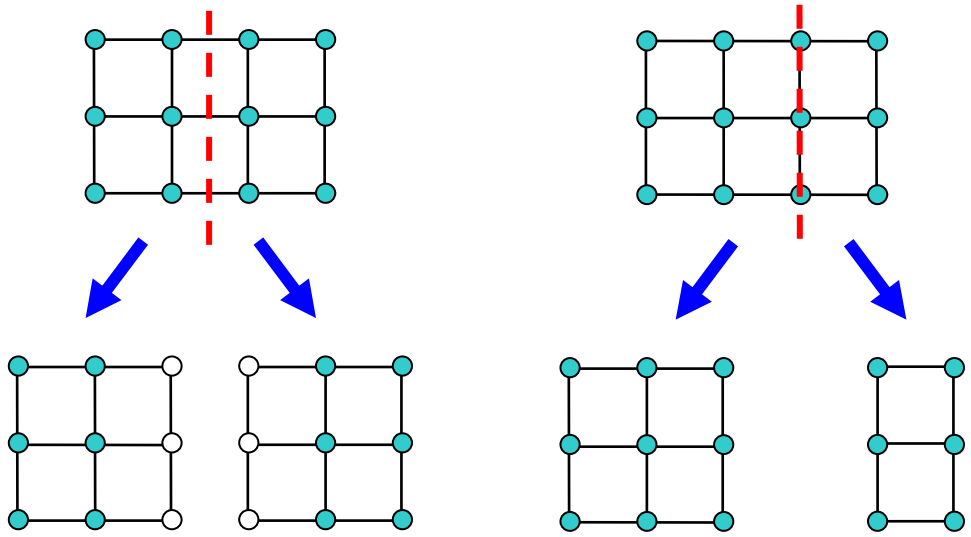

Fig. 1(a, left) Schematic of vertex based partitioning, (b, right) Schematic of element based partitioning.

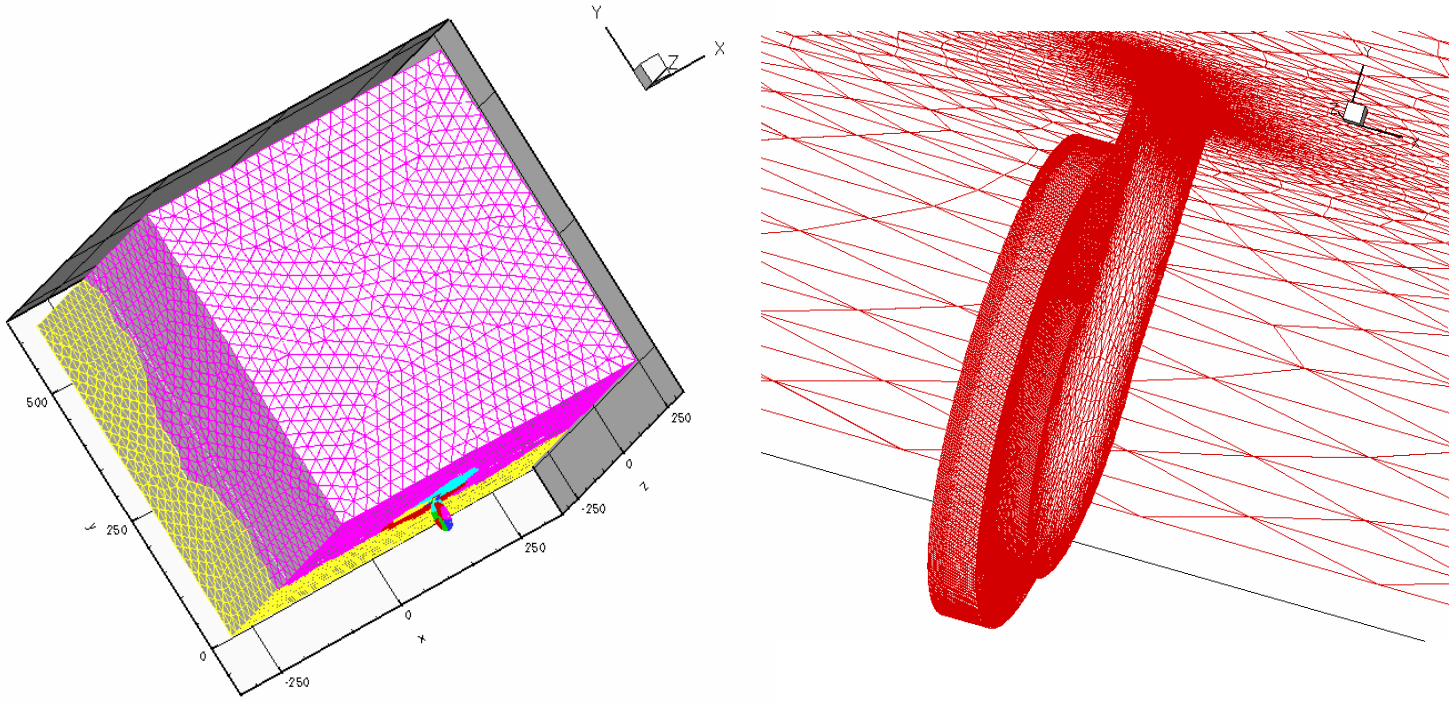

Fig 2 (a, left) a global view of the generated unstructured mesh (b, right) zoom-in picture of the actuator in unstructured grid mesh

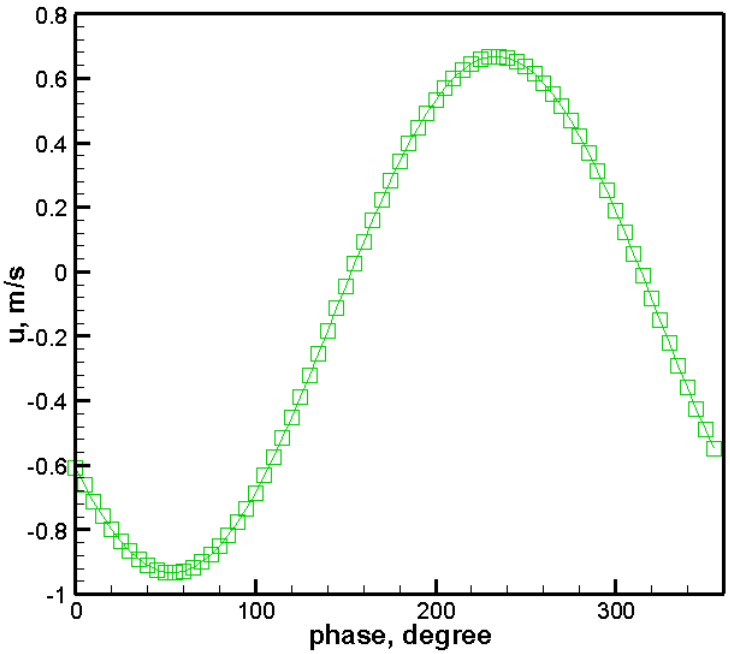

Fig. 3 The velocity profile of periodic boundary condition in one cycle.

CASE 1: TWO-DIMENSIONAL RANS SIMULATION OF SYNTHETIC JET FLOW FIELD

J. Cui[1] and R. K. Agarwal[2]

[1] *Graduate Research Assistant, Mechanical & Aerospace Engineering Department*
Washington University, St. Louis, MO 63130-4899
[2] *William Palm Professor of Engineering, Mechanical & Aerospace Engineering Department*
Washington University, St. Louis, MO 63130-4899

Introduction

A synthetic jet is generated by a piezoelectric diaphragm embedded on one side of a cavity. Flow enters and exits the cavity through an orifice in a periodic manner. Synthetic jets have been shown to exert significant control authority in many applications and have the additional benefit of being compact with zero net mass flux. During the past several years, many experimental and simulation studies have been reported in the literature to characterize the behavior of synthetic jets and their applications in flow control. However, there has not been a systematic study to assess the current capabilities of different classes of turbulent flow solution methodologies to predict flow fields induced by the synthetic jets. The purpose of this NASA Langley workshop [1] is to provide a systematic evaluation of various turbulent flow simulations methodologies by examining their performance against three experimental test cases.

Out of the three benchmark cases, Case 1: a synthetic jet issuing into the quiescent air, has been studied here by employing a 2D grid (4 zones, 35,986 grid points total). The simulations are performed by employing the computational code WIND-v.5 [2], which is a multi-zone structured-grid compressible Reynolds-Averaged Navier-Stokes (RANS) solver. Several turbulence models have been tested, such as Shear-Stress Transport (SST) [5], Spalart-Allmaras (SA) [4], SST combined with LES. The grid size and time-step independence have also been assessed. Comparisons with the experimental data show that the SST model gives the best results.

Solution Methodology

CFD code WIND is a product of the NPARC Alliance [2,3], a partnership between the NASA Glenn Research Center (GRC) and the Arnold Engineering Development Center (AEDC) dedicated to the establishment of a national, applications-oriented flow simulation capability. WIND computes the solution of the Euler and Navier-Stokes equations, along with supporting equation sets for turbulent and chemically reacting flows by employing a variety of turbulence models and chemistry models respectively. WIND is coded in Fortran 77, Fortran 90, and C programming languages. The governing equations are solved in conservation form. Explicit viscous terms are computed using either upwind or central differencing, and their order may be controlled through the use of keywords in the input data file. In all the simulation results presented here, the order of accuracy is second-order. The implicit convection terms are computed using either an approximate factorization scheme with four-stage Runge-Kutta time-stepping or they may be disabled altogether, and a global Newton iteration scheme may be employed. WIND uses externally generated computational grids. The solution is executed iteratively on this grid.

Model Description

As stated before, WIND is an Unsteady Reynolds-Averaged Navier-stokes (URANS) flow solver. WIND has various turbulence models: Spalart-Allmaras (SA) one-equation model [4] and Menter's Shear Stress Transport (SST) two-equation models [5, 6]. For unsteady flows, a combined SST and Large Eddy Simulation (LES) [7] model is also available. The combined model reduces to the standard SST model in high mean shear regions (e.g., near viscous walls), where the grid is refined and has a large aspect ratio unsuitable for LES models. As the grid is traversed away from high mean shear regions, it typically becomes coarser and more isotropic; the combined model smoothly transitions to an LES model. The intent is to improve predictions of complex flows in a real-world engineering environment, by allowing the use of LES methods with grids typical of those used with traditional Reynolds-Averaged Navier-Stokes solvers. An input parameter C_B (the default value 10.0 is used here) specifies the size of the RANS and LES zones. Increasing C_B increases the size of the region in which the combined model reduces to the standard SST model. All these three turbulence models (SA, SST, SST/LES) have been tested in our simulations presented in this paper.

Implementation and Case Specific Details

A two-dimensional grid is generated by a pre-processing Grid MANipulation (GMAN) code [8]. Zonal connectivity information is also computed by GMAN, and is stored in the grid file used by WIND. During the course of a solution, WIND maintains continuity in flow properties across zone boundaries through a process known as zone coupling [9]. The grid used in our simulations is shown in Fig. 1. It has 4 zones and 35,986 grid points. Zone 1 (33186) is the left side of cavity, zone 2 (62150) is the right side of cavity, zone 3 (41165) is the slot and zone 4 (1971139) is the external flow domain. In the external flow domain, there are 16 grid points from the wall (y=0) to a distance of y=0.1mm, which makes the resolution near the wall high enough to capture the features of the flow. Across the slot of the synthetic jet (in the x-direction), there are 41 points, which are enough to provide the accurate velocity profiles (u, v) across the slot.

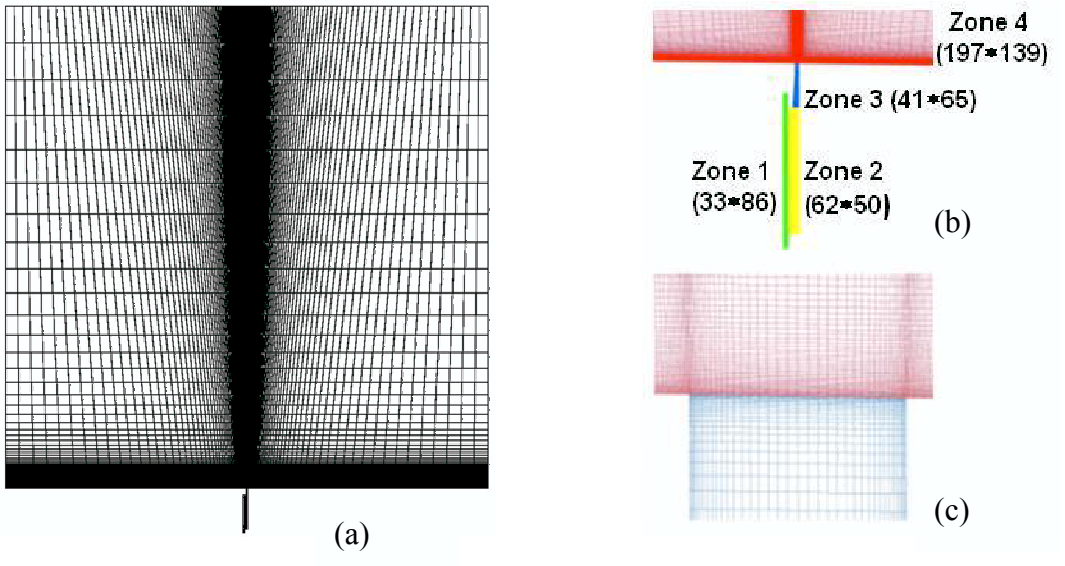

Figure 1: 2D grid used in the simulation
(a) Whole view (b) Configuration of four zones (c) Zoomed in view of the grid in the slot

All the boundary conditions are also specified in GMAN, and are stored in the grid file used by WIND. In the external flow domain (zone 4), the bottom wall is no-slip, from which the synthetic

jet ejects into the quiescent air. The other three boundaries of zone 4 (left, right and top) are specified as outflows. All the boundaries belonging to the cavity (zone 1, 2 and 3) are no-slip viscous walls, except the one where the diaphragm is located (I=1, zone 1). The "arbitrary inflow" is specified at this boundary as follows:

$$v(x, y \mid const, t) \mid 0 \tag{1}$$

$$u(x, y \mid const, t) \mid U \sin \varpi t \tag{2}$$

$$\psi \frac{\epsilon u}{\epsilon t} \mid 4 \frac{\epsilon p}{\epsilon x} \tag{3}$$

It is clear that the "mode shape" of the piezoelectric diaphragm is not simulated. Instead, it is modeled as a "piston", with velocity uniformly distributed in space. The volume change of the cavity is not included directly in the simulation either. It is found by numerical simulations that the net-mass-flux of the synthetic jet depends only on the pressure at the diaphragm, and not on the excitation velocity. Therefore, this pressure is tuned by calculating the mass-flux of the synthetic jet such that the net mass-flux is approximately zero. As shown in Fig. 2, when the pressure at the diaphragm is 14.709 psi, the relative net-mass-flux at the diaphragm is less than 1.0e-4, and the mass flux at the synthetic jet slot is also less than 1%.

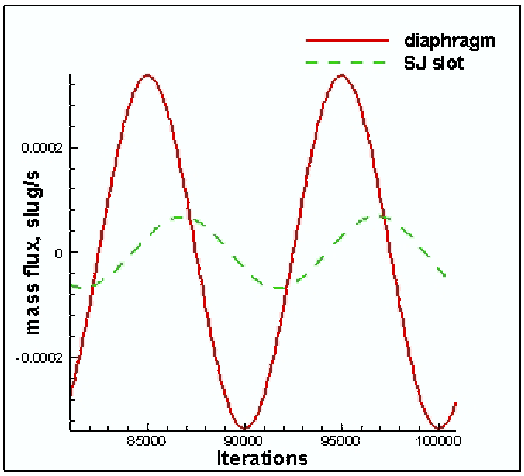

Figure 2: Mass-flux at the diaphragm & SJ slot

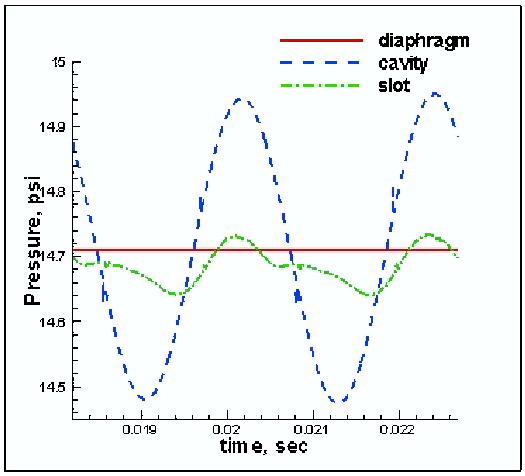

Figure 3: Pressure inside the cavity

After this pressure is determined, the velocity amplitude of the jet at the exit depends only on the velocity amplitude at the diaphragm. The excitation velocity at the diaphragm is determined to be 3.5 m/s. For incompressible flow, in Eq. (2), $U=U_J\ b/W$=0.8m/s, where U_J is the velocity amplitude of the synthetic jet, and W and b are the height of the diaphragm and the width of the jet-orifice respectively. Fig. 2 shows that the amplitude of mass flux at the slot is less than one-fourth of the amplitude of mass-flux at the diaphragm. This implies that the amplitude of velocity at the diaphragm is about four times 0.8 m/s, i.e. 3.2m/s. This 2D simulation assumes that the cavity is a cube. However in the experiment, the cavity is actually a cylinder. Thus, the volume ratio of the cavity to the orifice is not the same as in the experimental setup. Therefore, it is expected that the velocity used in the simulation here is not same as in the experiment.

Fig. 3 shows the pressure at three locations: the center of diaphragm, the center of the opposite side of diaphragm inside the cavity and at a location just above the jet-slot (x, y)=(0, 0.1mm). In the experiment, the pressure inside the cavity varies between 14.46 & 14.89 psi; it is between 14.47 & 14.95 psi in the simulation. Fig. 4 shows the calculated v-velocity at (x, y)=(0, 0.1mm), which is in good agreement with the PIV & Hotwire data. These observations justify that the boundary conditions employed at the diaphragm in our 2D simulation are applicable to define the

experimental set-up, since the computed flow inside the cavity and at the slot behaves in a manner very similar to that in the experiment.

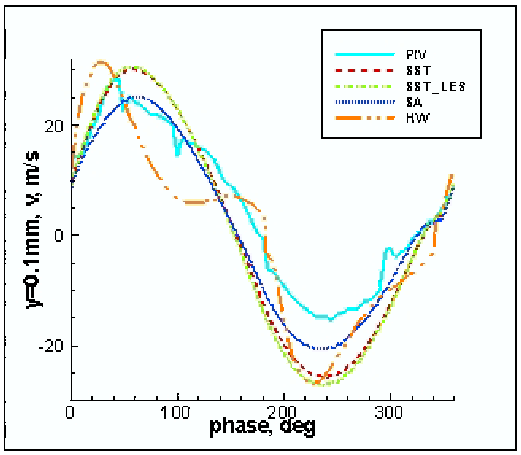

Figure 4: Phase-averaged *v*-velocity at (x, y) = (0, 0.1 mm)

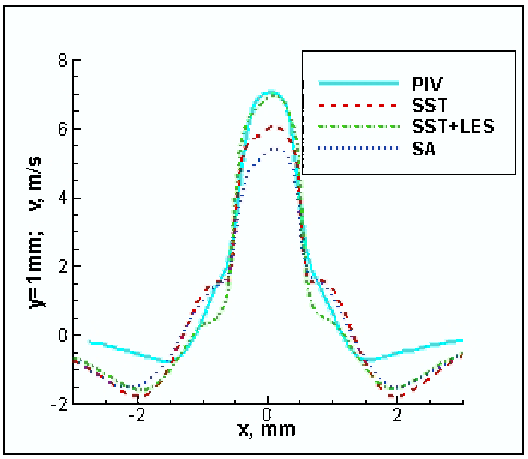

Figure 5: Long-time averaged *v*-velocity at (x, y) = (0, 1 mm)

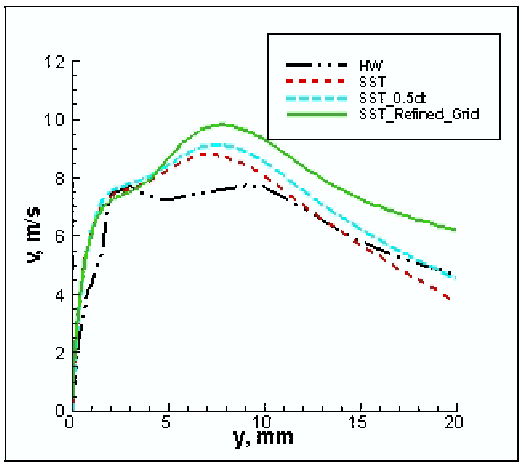

(a) Long-time averaged *v*-velocity along the centerline

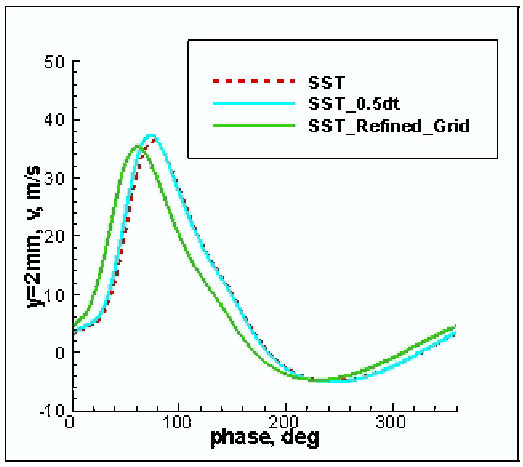

(b) Phase-averaged *v*-velocity at (0, 2mm)

Figure 6: Time-step and grid independence studies; dt = time-step

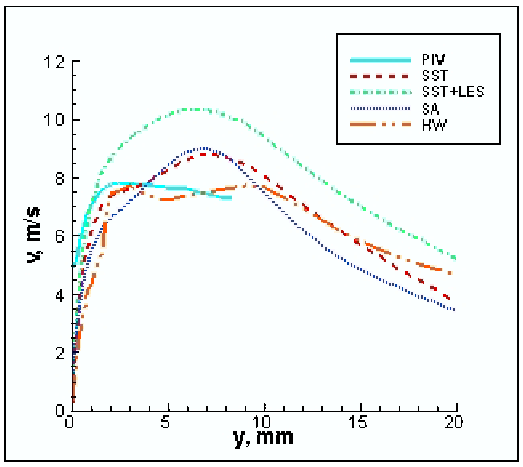

(a) *v*-velocity along the centerline

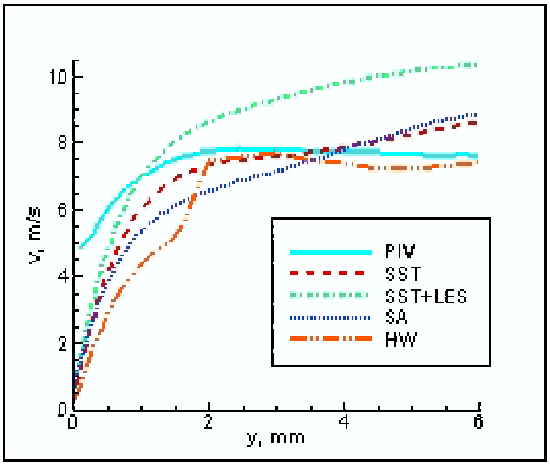

(b) Zoomed-in view: near the wall

Figure 7: Long-time averaged *v*-velocity along the centerline of SJ.

The results presented in Figs. 2-4 have been obtained by using a time step corresponding to 10000 steps per SJ cycle. The time-step therefore is 1/444.7 (Hz)/10000 = 2.3486e-7(sec). Time step & grid independence studies were conducted by using a half time step and half grid spacing in y direction. Fig. 6 shows the long-time averaged v-velocity along the centerline and phase-averaged v-velocity at (x= 0, y= 2 mm). Both Figs. 6(a) and 6(b) show the effect of time-step and grid refinement on the solution using a SST turbulence model.

Different turbulence models have also been tested. Fig. 7 shows the variation of v-velocity along the centerline using the SST, SST_LES, and SA models, and comparison of calculations with the PIV and hotwire (HW) data. There is noticeable discrepancy between the PIV and HW data. Near the jet exit, all the simulation results lie between the PIV and HW measurements. In the range y=10 to 20mm, simulated v-velocity is very close to the HW data, except for the SST combined with LES model, which over-estimates the velocity. The maximum velocity in the experiment is 7.8 m/s. It is about 9 m/s in most of the simulations. The maximum velocity appears near the wall in the experiment, but not in simulations. Fig. 5 shows the computed long-time averaged v-velocity at (x, y) = (0, 1 mm). Again, there is a good agreement with PIV data.

Based on the above comparisons, we conclude that the URANS simulation with SST model, with 10000 time steps per synthetic jet cycle, gives the best results for this case.

References

[1] http://cfdval2004.larc.nasa.gov/

[2] http://www.grc.nasa.gov/WWW/winddocs/index.html

[3] Bush, R.H., “The Production Flow Solver of the NPARC Alliance,” AIAA Paper 88-0935, 1988.

[4] Spalart, P. R. and Allmaras, S. R., “A One-Equation Turbulence Model for Aerodynamic Flows," AIAA Paper 92-0439, 1992.

[5] Menter, F.R., “Zonal Two-Equation k-ϖ Turbulence Models for Aerodynamic Flows,” AIAA Paper 93-2906, 1993.

[6] Mani, M., Ladd, J. A., Cain, A. B., and Bush, R. H., “An Assessment of One- and Two-Equation Turbulence Models for Internal and External Flows," AIAA Paper 97-2010, 1997.

[7] Spalart, P. R., Jou, W. H., Strelets, M., and Allmaras, S. R., “Comments on the Feasibility of LES for Wings, and on a Hybrid RANS/LES Approach," First AFOSR International Conference On DNS/LES, Aug. 4-8, 1997, Ruston, Louisiana. In “Advances in DNS/LES,” Liu, C. and Liu, Z., eds., Greyden Press, Columbus, Ohio, 1997.

[8] http://www.grc.nasa.gov/WWW/winddocs/gman/index.html

[9] Romer, W. W. and Bush, R. H., "Boundary Condition Procedures for CFD Analyses of Propulsion Systems - The Multi-Zone Problem," AIAA Paper 93-1971, 1993.

CASE 1: TIME-ACCURATE NUMERICAL SIMULATIONS OF SYNTHETIC JETS IN QUIESCENT AIR

K-A. B. Rupesh[1], B. R. Ravi[1], R. Mittal[1], R. Raju[1], Q. Gallas[2], and L. Cattafesta[2]

[1]*Department of Mechanical & Aerospace Engineering,*
The George Washington University, Washington, DC 20052.
[2]*Department of Mechanical & Aerospace Engineering,*
University of Florida, Gainesville, FL 32611.

Introduction

The unsteady evolution of three-dimensional synthetic jet into quiescent air is studied by time-accurate numerical simulations using a second-order accurate mixed explicit-implicit fractional step scheme on Cartesian grids. Both two-dimensional and three-dimensional calculations of synthetic jet are carried out at a Reynolds number (based on average velocity during the discharge phase of the cycle $V_{j,}$ and jet width d) of 750 and Stokes number of 17.02. The results obtained are assessed against PIV and hotwire measurements provided for the NASA LaRC workshop on CFD validation of synthetic jets.

Numerical Methodology

The evolution of zero-net mass-flux synthetic jet from a cavity into quiescent air is modeled by the unsteady, incompressible Navier-Stokes equations, written in tensor form as

$$\frac{\partial u_i}{\partial x_i} = 0; \quad \frac{\partial u_i}{\partial t} + \frac{\partial u_i u_j}{\partial x_j} = -\frac{\partial p}{\partial x_i} + \frac{1}{\mathrm{Re}} \frac{\partial^2 u_i}{\partial x_j \partial x_j}$$

where the indices, $i = 1, 2, 3,$ represent the x, y and z directions, respectively; while the velocity components are denoted by u (u_1), v (u_2) and w (u_3), respectively. The equations are nondimensionalized with the appropriate length and velocity scales where Re represents the Reynolds number. The Navier-Stokes equations are discretized using a cell-centered, collocated (non-staggered) arrangement of the primitive variables ($\vec{u}$, p). In addition to the cell-center velocities ($\vec{u}$), the face-center velocities, $\vec{U}$, are also computed. Similar to a fully staggered arrangement, only the component normal to the cell-face is calculated and stored. The face-center velocity is used for computing the volume flux from each cell. The advantage of separately computing the face-center velocities has been discussed in the context of the current method in Ye *et al.* [1]. The equations are integrated in time using the fractional step method. In the first step, the momentum equations without the pressure gradient terms are first advanced in time. In the second step, the pressure field is computed by solving a Poisson equation. A second-order Adams-Bashforth scheme is employed for the convective terms while the diffusion terms are discretized using an implicit Crank-Nicolson scheme which eliminates the viscous stability constraint. The pressure Poisson equation is solved with a Krylov-based approach.

The solver uses a multi-dimensional ghost-cell methodology to incorporate the effect of the immersed boundary on the flow; however, the absence of curvilinear topology in the geometry makes this approach unnecessary in the current study. Care has been taken to ensure that the discretized equations satisfy local and global mass conservation constraints as well as pressure-velocity compatibility relations. The code has been rigorously validated by comparisons against established experimental and computational data. Details have been presented elsewhere [2, 3].

Implementation and Case Specific Details

The present study models the flow inside the cavity using a pulsatile velocity boundary condition, $v = v_o \sin(\omega t)$ prescribed at the bottom of the cavity (see Fig. 1) in order to generate a natural flow at the slot exit. The shape of the cavity is approximated to be a rectangular box without taking into consideration the finer details that make up the interior of the cavity. However, the geometrical and flow parameters used in the current study are chosen based on a scaling analysis of various parameters involved like slot width *(d)*, slot height *(h)*, cavity width *(W),* cavity height *(H),* the diaphragm vibrating frequency *(f),* etc.. For instance, the slot size is chosen such that the ratio *h/d* and *W/d* match those used in the experiments; however, *H/d* of 4.95 used in the calculations is not matched in the experiments. The Reynolds number (Re) in this work is defined based on average jet velocity during the discharge phase of the cycle *(V_j)* and jet width (d) i.e., $\mathrm{Re} = V_j d / \upsilon$. Average jet velocity *(V_j)* in the numerical calculations is set equal to the value of 10.5 *m/s,* obtained by averaging the velocity provided by the LDV measurements during the discharge phase of the cycle. Because of the uncertainty in V_j reported by different measurements, a nominal Re of 750 corresponding to the lower bound of V_j calculated from the measurements is chosen in the present investigation. Experimental values of ω = 2794 *rad/s,* d = 1.27 *mm and* υ = 1.5527x10^{-5} m^2/s are matched to give a Stokes number ($S = \sqrt{\omega d^2 / \upsilon}$) of 17.02 in the computations. Various cases considered in the present study and the corresponding flow parameters are detailed in Table 1.

#	*Re*	2D/3D	*S*	Exterior Domain Size	Grid Size	Time steps/cycle N	$\Delta t = \frac{2\pi}{\omega N}$
1.	750	3D	17.02	30dx 30d x 3d	132x250x 16	14,000	0.00116144
2.	750	2D	17.02	30d x 30d	132 x 220	14,000	0.00116144

Table 1.Various cases considered in the study and their flow parameters.

Figure 1 shows the schematic of the computational domain and the boundary conditions used in the computations. An outflow velocity boundary condition is prescribed at the left, right and top boundaries that allow them to respond freely to the flow created by the jet. In 3D calculations, periodic boundary conditions are prescribed in the span wise *(z)* direction. Figure 2 shows an *x-y* slice of a typical 3D mesh used in the region near the slot in the computations. Grids used in the current work are non-uniform in both *x-* and *y-*directions, and uniform in the span wise *(z)* direction in the case of 3D calculations.

Sufficient clustering is provided in the slot-region along *x*- and *y*-directions to resolve the vortex structures that form at the slot exit, as well as the shear layer in the slot. Typically 32 grid points clustered using a cosine-hyperbolic distribution are used across the slot. In 3D calculations, the three-dimensionality in the solution is instigated by introducing a small sinusoidal spatial perturbation in the z-component of velocity *(w)* over a few hundred time-steps in the first cycle. For all cases presented here, the first two cycles of calculations are not included in the averaging process to eliminate transient effects, and the next two to three cycles are used in the process.

Results

Figure 3 shows the isosurfaces of vorticity magnitude obtained from three-dimensional calculation before the onset of full three-dimensionality in the solution. It is clear from the figure that the flow is dominated by counter-rotating vortex pairs. Figure 4 shows the isosurfaces of vorticity magnitude for the same solution after the onset of full three-dimensionality. Figure 4 shows two pairs of rib vortices along the span obtained from the 3D simulation. The plot of phase-averaged *v*-velocity component vs. phase angle ϕ at the point (*x, y*) = (0 *mm,* 0.1 *mm*) shown in Figure 5 describes the procedure involved in aligning the CFD data with PIV data. Phase angle at which $V_{avg} = (V_{max+} V_{min})/2$ intersects the curve is made 340^o by applying the required phase shift. Figure 6 shows the plot of phase-averaged *v*-velocity component vs. phase angle ϕ at the point (*x, y*) = (*0 mm, 0.1 mm*) for the two calculations and it can be seen that the CFD data is reasonably aligned with the PIV data. Plot of time-averaged *u*- and *v*-velocity components at the point (*x, y*) = (*0 mm, 0.1 mm*) across the slot region is shown in Figure 7. Figure 8 and 9 show the comparison of phase-averaged *u*- and *v*-velocity components at the same point at $\phi = 90^o$ and $\phi = 270^o$ respectively. Three-dimensional calculations at Re > 1000 corresponding to the upper bound of V_j reported in the experiments are being carried out and since the solutions at these Reynolds numbers were not converged at the time of preparation of this report, they would be presented in detail at the workshop.

Acknowledgements
This work is supported by NASA (Grant NAG-1-01024) and AFOSR (Grant F49620-03-1-0146 and F49620-03-1-0135).

References

[1] Ye, T., Mittal, R., Udaykumar, H. S. and Shyy, W., "An Accurate Cartesian Grid Method for Viscous Incompressible Flows with Complex Immersed Boundaries," *J. Comp. Phys.* Vol. 156, pp. 209-240, 1999.

[2] Ravi, B. R., Mittal, R., and Najjar, F. M., "Study of Three-Dimensional Synthetic jet Flowfields Using Direct Numerical Simulation," *AIAA 2004-0091,* 2004.

[3] Najjar, F.M., and Mittal, R., "Simulations of Complex Flows and Fluid-Structure Interaction Problems on Fixed Cartesian Grids," *FEDSM 2003-45577*, Proceedings of FEDSM'03, 4th ASME-JSME Joint Fluids Engineering Conference, July 6-11, Honolulu, Hawaii, 2003

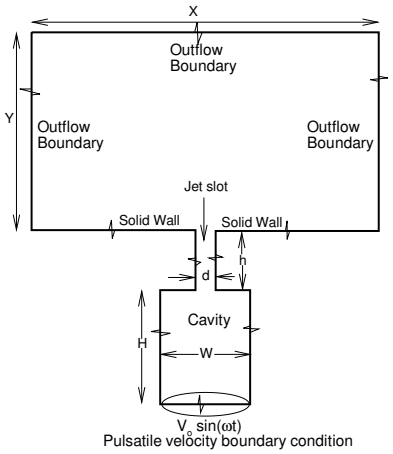

Figure 1: Schematic of the computational domain and boundary conditions.

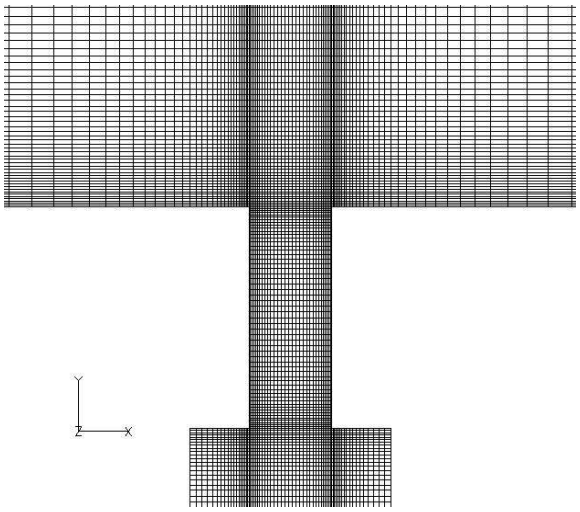

Figure 2: A typical grid in the slot region used in the computations.

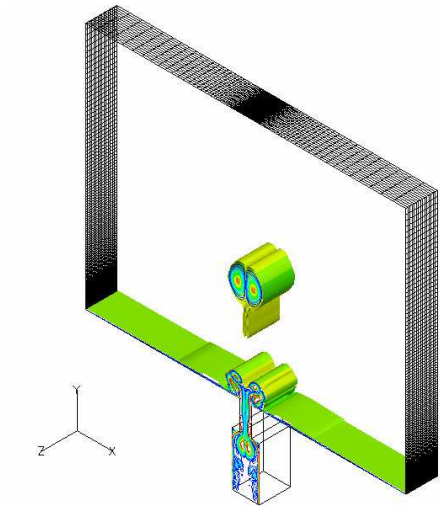

Figure 3: Isosurfaces of vorticity magnitude 2nd cycle, Re = 750, S = 17.02.

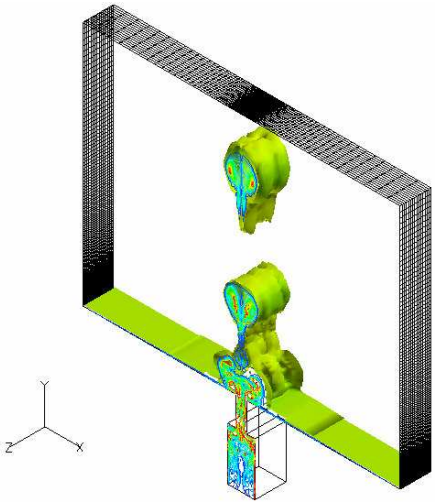

Figure 4: Isosurfaces of vorticity magnitude 3rd cycle, Re = 750, S = 17.02

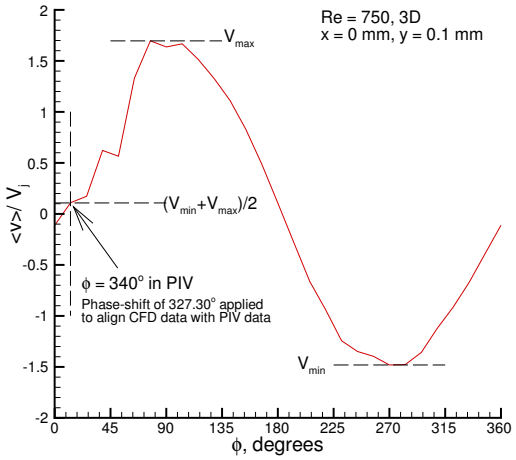

Figure 5: Plot of phase-averaged v vs. phase angle before aligning CFD data with PIV data.

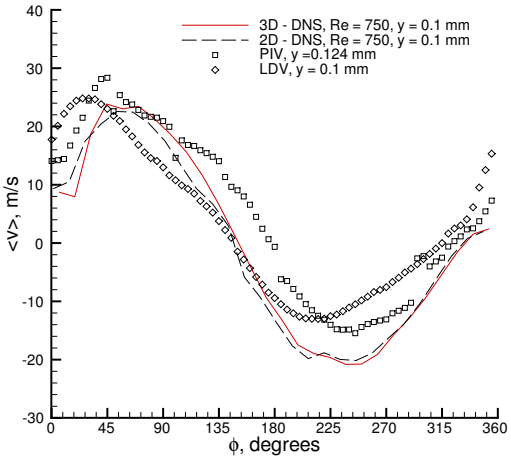

Figure 6: Plot of phase-averaged v vs. phase angle after aligning CFD data with PIV data.

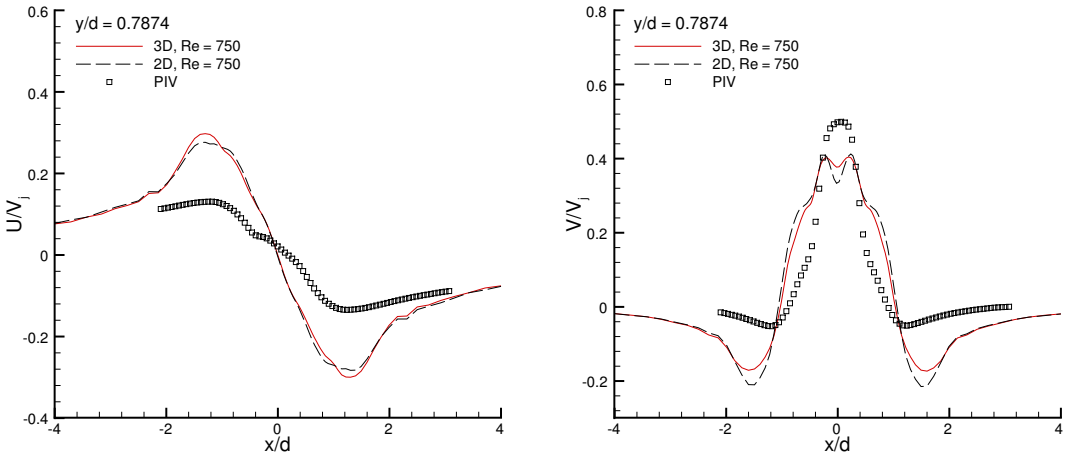

Figure 7: Plot of time-averaged u- and v-velocities along the horizontal line y = 0.7874 (≈1mm in the experiments).

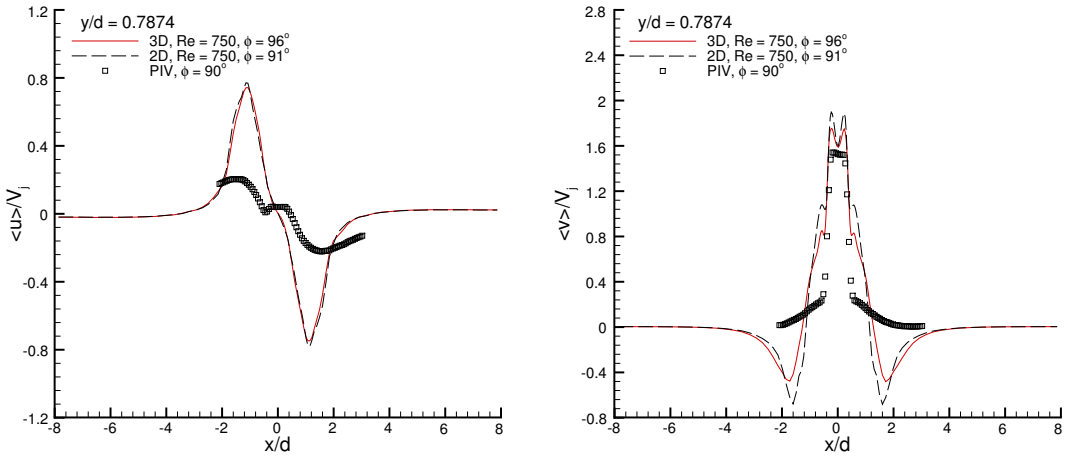

Figure 8: Plot of phase-averaged u- and v-velocities along the horizontal line y = 0.7874 (≈1mm in the experiments) at $\phi = 90^{o}$ degrees.

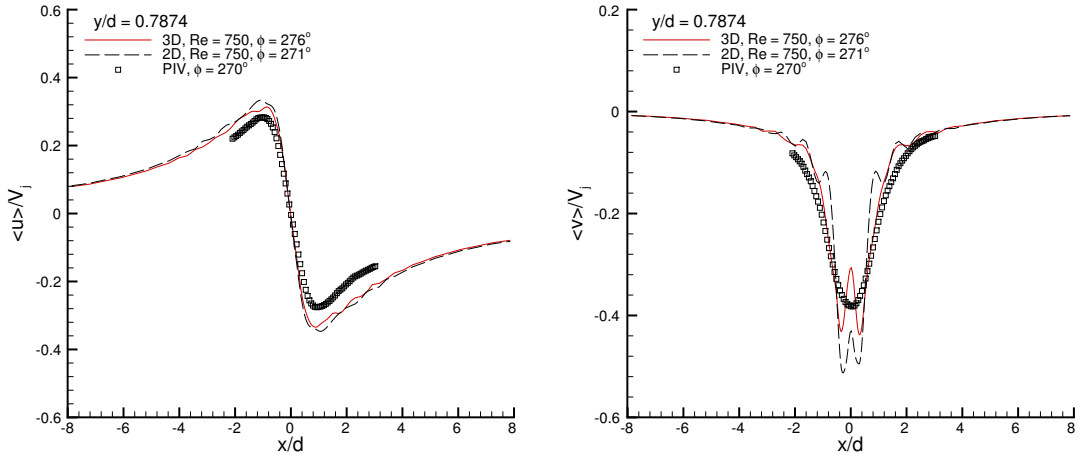

Figure 9: Plot of phase-averaged u- and v-velocities along the horizontal line y = 0.7874 (≈1mm in the experiments) at $\phi = 270^{o}$ degrees.

CASE 1: A REDUCED-ORDER MODEL FOR ZERO-MASS SYNTHETIC JET ACTUATORS

Nail. K. Yamaleev[1], Mark H. Carpenter[2], and Veer S. Vatsa[2]

[1]*Department of Mathematics, North Carolina A&T State University, Greensboro, NC 27410*
[2]*Computational Modelling & Simulation Branch, NASA Langley Research Center, Hampton, VA 23681*

Introduction

Accurate details of the general performance of fluid actuators is desirable over a range of flow conditions, within some predetermined error tolerance. Designers typically model actuators with different levels of fidelity depending on the acceptable level of error in each circumstance. Crude properties of the actuator (e.g., peak mass rate and frequency) may be sufficient for some designs, while detailed information is needed for other applications (e.g., multiple actuator interactions).

This work attempts to address two primary objectives. The first objective is to develop a systematic methodology for approximating realistic 3-D fluid actuators, using quasi-1-D reduced-order models. Near full fidelity can be achieved with this approach at a fraction of the cost of full simulation and only a modest increase in cost relative to most actuator models used today. The second objective, which is a direct consequence of the first, is to determine the approximate magnitude of errors committed by actuator model approximations of various fidelities. This objective attempts to identify which model (ranging from simple orifice exit boundary conditions to full numerical simulations of the actuator) is appropriate for a given error tolerance.

Solution Methodology

The solution methodology used for this work is described in detail elsewhere [1]. Only the general aspects of the approach will be replicated herein. The time-dependent 2-D Navier-Stokes equations are used to describe the unsteady compressible flow generated by a synthetic jet actuator. No turbulence model is used in these simulations. The governing equations in curvilinear coordinates (ξ, η) are written in conservation law form. All the length scales and dependent variables have been nondimensionalized by the orifice width d and the corresponding reference values, respectively, except for p which has been normalized by $\rho_\infty u_\infty^2$, where u_∞ has been chosen to be one tenth of the speed of sound. The viscosity coefficient μ is assumed to be constant, and the equation of state for a perfect gas is used to relate pressure to the conservation variables.

The governing equations are closed with the following boundary conditions. A no-slip boundary condition for the velocity vector and a constant wall temperature are imposed on the wall surface

$$u|_{wall} = v|_{wall} = 0, \quad T|_{wall} = T_\infty. \tag{1}$$

At the subsonic outflow boundary, a boundary condition for the pressure is imposed weakly. Characteristic conditions are applied at the upper boundary so that the vortex structures can leave the computational domain without producing perceptible spurious reflections. The unsteady flow inside the actuator cavity, generated by harmonic motion of the diaphragm, is modeled by using a new reduced-order model described in the next section.

The actuator geometry is represented as the summation of multiple subdomains, each having a high degree of smoothness. Within each subdomain, a computational grid is generated having sufficient smoothness

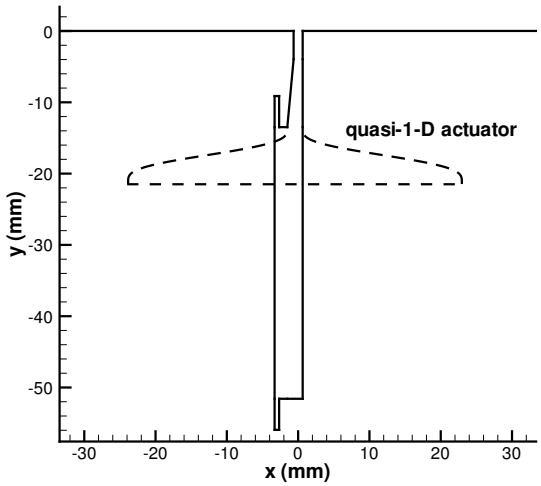

Figure 1: The 2-D and quasi-1-D geometries.

to allow solutions with three significant digits of accuracy. The connectivity at the subdomain interfaces is C_0 smooth: thus meshlines connect at interfaces but need not have smooth derivatives.

Two distinct geometries are the focus of the study. The first is a simple 2-D projection of the 3-D actuator used in Case I. The 2-D geometry of the actuator is not the centerline cut of the actual geometry, but rather is adjusted slightly so that the volume of the 2-D actuator (assuming a constant width of 1.24") is precisely that of the 3-D actuator. This was done because the volume of the actuator strongly affects the resonance characteristics of the device. The exterior portion is truncated at 100 orifice diameters. The second geometry is a subset of the first, but only includes the exterior portion of the device and the nozzle portion of the actuator. The rest of the actuator is approximated with the reduced order model, by solving the quasi-1-D Euler equations. The volume of the quasi-1-D actuator has also been chosen to be equal to the corresponding volume of the 3-D actuator. Both the 2-D and quasi-1-D geometries are shown in Fig. 1. The region where the quasi-1-D model is used is bounded by the dashed line, whereas in the rest of the domain, the 2-D Navier-Stokes equations are solved.

The grid was adjusted within the actuator and in the nearfield of the exterior to achieve two significant digits in the solution accuracy. The exterior grid was sufficient in resolution to accurately resolve the vortices near the orifice and up to ten diameters away from the orifice. Beyond that point, the mesh was expanded and the vortices were allowed to diffuse. The total number of grid points in the full 2-D and quasi-1-D simulations were 60,697 and 38,805, respectively.

A fourth-order upwind-biased linear finite difference scheme based on the local Lax-Friedrichs flux splitting is used to discretize both the 2-D Navier-Stokes equations and the quasi-1-D Euler equations. For sufficient grid smoothness within each 2-D subdomain, design order accuracy is achieved. The interfaces are connected using the penalty approach (SAT) described in detail in references [2, 3, 4, 1]. The interface penalty treatment is conservative, and maintains the underlying accuracy of the interior scheme. The SAT procedure requires co-located solution variables on both sides of the interface. The difference between the two solution values was used as a measure of spatial grid resolution. For all the simulations, the interface error was less than 0.5%.

The semi-discrete equations were explicitly integrated in time with a low-storage 4th-order Runge-Kutta scheme [5]. The simulations were all run at the maximum stable timestep. The temporal scheme has an error estimator that monitors the temporal error per timestep. The timestep error varied over the period in the range $10^{-10} - 10^{-7}$, based on the L_∞ norm of the density variable. Other solution variables had similar error norms. Each cycle required about 10^5 timesteps to complete.

Model Description

A gap exists between the 0-D models and the full 2-D/3-D models of a synthetic jet actuator. To combine the accuracy and conservation properties of the full numerical simulation methods with the efficiency of the simplified blowing/suction type boundary conditions, a new reduced-order model of a multidimensional synthetic jet actuator is proposed. In contrast to the methods available in the literature, the new approach uses a reduced-order model to approximate a 2-D or 3-D actuator. The multidimensional actuator is simulated by solving the time-dependent quasi-1-D Euler equations. The time-dependent quasi-1-D Euler equations can be written in the following conservation law form:

$$\frac{\partial \mathbf{U}}{\partial t} + \frac{\partial \mathbf{E}}{\partial y} + \mathbf{H} = 0, \tag{2}$$

$$\mathbf{U} = A \begin{bmatrix} \rho \\ \rho v \\ \rho e \end{bmatrix}, \quad \mathbf{E} = A \begin{bmatrix} \rho v \\ \rho v^2 + p \\ v(\rho e + p) \end{bmatrix}, \mathbf{H} = - \begin{bmatrix} 0 \\ p\frac{\partial A}{\partial y} \\ 0 \end{bmatrix},$$

where A is the cross-sectional area of the quasi-1-D actuator. It is assumed that A is a continuously differentiable function that is independent of time, i.e., $A = A(y)$.

To simulate the diaphragm dynamics, a time-dependent one-to-one coordinate transformation,

$$\begin{aligned} \tau &= t \\ \zeta &= \zeta(t, y), \end{aligned} \tag{3}$$

is employed to map a physical domain with the moving boundary onto a unit interval. Note that the ζ coordinate depends on time and, therefore, a moving mesh technique is applied to solve the quasi-1-D Euler equations. Because the frequency of diaphragm oscillations ω is a given quantity, the moving mesh can be generated analytically

$$y(\zeta, \tau) = (1 - \zeta)\left[L + a(1 - \cos(\omega\tau))\right], \tag{4}$$

where y and ζ are physical and computational coordinates, respectively, a and ω are the amplitude and frequency of diaphragm oscillation, and $L + a$ is a mean depth of the quasi-1-D synthetic jet actuator.

Diaphragm oscillations are forced by varying the position of the diaphragm $y(0, \tau)$ where the impermeable wall boundary condition is imposed. Because the deforming mesh Eq. (4) is given analytically, the diaphragm velocity can be calculated by differentiating Eq. (4) with respect to time to give

$$v(0, \tau) = a\omega \sin(\omega\tau). \tag{5}$$

It should be noted that the region near the jet exit requires special consideration. The full numerical simulation of the actuator orifice region is crucial for accurate prediction of the interaction between the synthetic jet and the external boundary layer. This region is characterized by strong flow separation that cannot be described by the quasi-1-D Euler equations. To overcome this problem, the quasi-1-D actuator model is used only to simulate the flow inside the actuator cavity, while the small region near the actuator orifice is modeled by solving the 2-D unsteady Navier-Stokes equations. This approach allows us to accurately predict the interaction of the synthetic jet with the external boundary layer and to resolve vortices generated in the vicinity of the actuator orifice, while reducing the computational cost.

The low-dimensional actuator model has several advantages. First, this approach is fully conservative and provides conservation of mass, momentum, and energy. Second, the new quasi-1-D model is computationally much more efficient compared with the 2-D or 3-D numerical simulation of the cavity flow. Third, the reduced-order model retains some important multidimensional features of the realistic actuator, such as the length, diaphragm deflection, and area variation. These properties of the new model and its ability to account for the compressibility effects inherent in actuator devices make it an efficient tool for quantitative study of the actuator resonance characteristics.

To demonstrate the ability of the new reduced-order model to quantitatively predict the 3-D actuator dynamics, the phase-averaged time history of vertical velocity over the center of the slot obtained with the quasi-1-D model and three different measurement techniques is shown in Fig. 2.

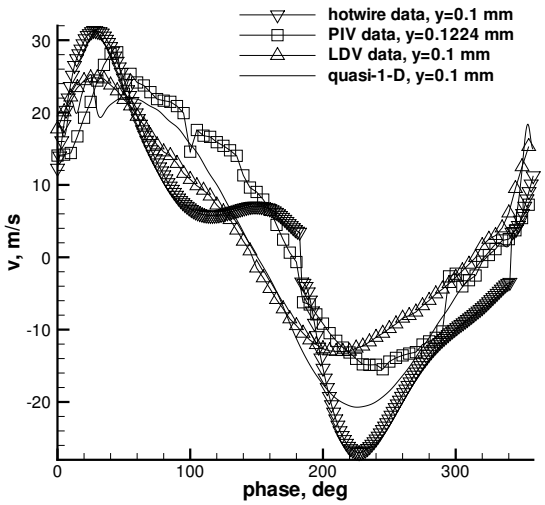

Figure 2: Phase-averaged time-history of the vertical velocity over the center of the slot, obtained with the quasi-1-D model and using the PIV, hotwire, and LDV measurement techniques.

Implementation and Case Specific Details

The simulations were started with quiescent flow and run through sufficient periods to obtain periodic solutions. This was usually about 10 periods. The experimentally determined diaphragm position was used to describe the moving boundary condition of the quasi-1-D actuator. The shape of the diaphragm was assumed to be the first mode of the Bessel function eigensolution of the cylindrical dram symmetric vibration. A scaling factor of 1.35 was later added to obtain the peak exit velocity that was in the Mach = 0.1 range.

Acknowledgments

The work of the first author was partially funded by NASA Langley Research Center and NIA.

References

[1] N.K. Yamaleev, M.H. Carpenter, A Reduced-Order Model for Efficient Simulation of Synthetic Jet Actuators, NASA/TM-2003-212664, December 2003, (submitted to AIAA Journal).

[2] M.H. Carpenter, D. Gottlieb, and S. Abarbanel, Time-Stable Boundary Conditions for Finite Difference Schemes Solving Hyperbolic Systems: Methodology and Application to High Order Compact Schemes, *Journal of Computational Physics*, Vol. 111, No. 2, April 1994.

[3] M.H. Carpenter, Jan Nordström, D. Gottlieb, A stable and Conservative Interface Treatment of Arbitrary Spatial Accuracy *Journal of Computational Physics*, Vol. 148, 341-365, (1999).

[4] J. Nordström, M.H. Carpenter, Boundary and Interface Conditions for High-Order Finite-Difference Methods Applied to the Euler and Navier-Stokes Equations *Journal of Computational Physics*, Vol. 148, 621-645, (1999).

[5] M.H. Carpenter, C.A. Kennedy, Fourth-Order 2N-Storage Runge-Kutta Schemes, NASA-TM-109112, April 1994.

CASE 1: Lumped Element Modeling

Quentin Gallas,[§] Rajat Mittal,[‡] Mark Sheplak[†] and Louis Cattafesta[†]

[†]*Department of Mechanical & Aerospace Engineering, University of Florida, Gainesville, FL 32611-6250*
[‡]*Department of Mechanical & Aerospace Engineering, George Washington University, Washington, DC 20052*

[§]*Graduate Student*
[†‡]*Associate Professor*

Introduction

The approach described here is to model the response of a synthetic jet using lumped element modeling to complement more rigorous and expensive numerical simulations.

Solution Methodology

The approach used is to model the actuator orifice impedance without a grazing boundary layer and is based on a lumped element modeling (LEM) technique, following the recent paper by Gallas et al. [1].

Model Description

In LEM, the individual components of a synthetic jet are modeled as elements of an equivalent electrical circuit using conjugate power variables (i.e., power = generalized "flow" x generalized "effort" variables). Figure 1 shows an equivalent circuit representation of a piezoelectric-driven synthetic jet actuator, where the lumped parameters represent generalized energy storage elements (i.e., capacitors and inductors) and dissipative elements (i.e., resistors). Model parameter estimation techniques, assumptions, and limitations are discussed in Gallas et al. [1]. The frequency response function of the circuit is derived to obtain an expression for Q_{out}/V_{ac}, the volume flow rate during the expulsion part of the cycle per applied voltage. LEM provides a compact nonlinear analytical model and valuable physical insight into the dependence of the device behavior on geometry and material properties.

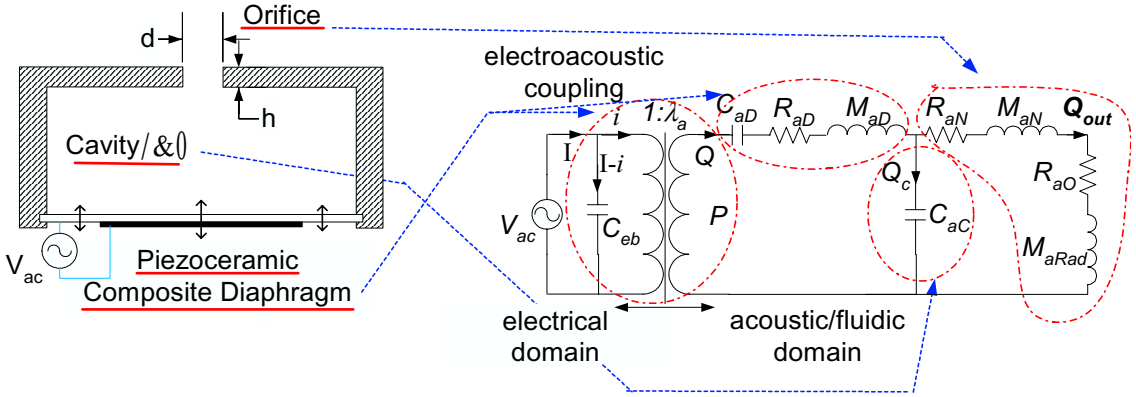

Figure 1: Equivalent circuit model of a piezoelectric-driven synthetic jet actuator.

With slight modifications, the model is applicable to any type of zero-net mass flux actuator, (piezoelectric, voice-coil, etc.) and also for two-dimensional slots and axisymmetric orifices. Case 1 is similar to the device studied and modeled by Gallas et al. [1], namely a piezoelectric-driven synthetic jet exhausting into a quiescent medium through a circular orifice.

The various lumped parameters shown in Figure 1 are fully described in Gallas et al. [1]. The only empirical constant is the structural damping ratio for the acoustic diaphragm resistance, R_{aD}. Simple analytical expressions are available for all other elements. The only difference for the current case from that considered in [1] comes from the expressions for the orifice impedance due to the use of a rectangular slot. Using the same approach described in [1], the acoustic resistance of the orifice is obtained for low frequencies assuming fully-developed laminar channel flow in a slot of width *d*, height *h* and length *w*

$$R_{aN} = \frac{\div P_{out}}{Q_{out}} = \frac{3\sigma h}{2w/d/2)^3}, \tag{1}$$

where σ is the dynamic viscosity of the fluid and Q_{out} is the volume flow rate produced by the differential pressure $\div P_{out}$ across the slot. The acoustic mass in the slot is obtained by integrating the distributed kinetic energy and equating it to the lumped kinetic energy,

$$M_{aN} = \frac{3\psi h}{5w/d/2)}. \tag{2}$$

The acoustic radiation mass M_{aRad} is modeled for $kd \{ 1$ as a rectangular piston in an infinite baffle by assuming that the rectangular slot is mounted in a plate that is much larger in extent than the slot size,

$$X_{aRad} = j\varpi M_{aRad} = \frac{\psi c_0}{dw} k \left(\frac{w}{\phi \ln/2d/w)} 2 \frac{d}{2\phi/1 4 k^2 w^2/6)} \right), \tag{3}$$

where X_{aRad} corresponds to the acoustic radiation reactance, $k = \varpi/c_0$ is the wave number, and c_0 is the isentropic speed of sound, ϖ is the radian frequency, and $j = \sqrt{41}$.

Implementation and Case-Specific Details

LEM provides the frequency response of the actuator for a given input voltage. Since the orifice/slot acoustic resistance is nonlinear, the frequency response is a function of the input voltage amplitude. As discussed in Gallas et al. [1], a piezoelectric-driven synthetic jet actuator exhibits two resonant frequencies. A definition of the various frequencies used hereafter is given below:

$f_{\exp}$ = 444.7 Hz = drive frequency of the diaphragm used in the experiment

f_D = 460.2 Hz = calculated natural frequency of the diaphragm, determined from linear composite plate theory [2]

f_H = 1911.7 Hz = Helmholtz resonant frequency of the cavity $f_H = 1/2\phi\sqrt{/M_{aN} 2 M_{aRad})C_{aC}}$

f_1 = 445.1 Hz = calculated first resonant peak of the entire system

f_2 = 1976.9 Hz = calculated second resonant peak of the entire system

The relationship between the frequencies is given by $f_1 f_2 = f_D f_H$, but $f_1 \Pi f_D$ and $f_2 \Pi f_H$. In order to successfully model the piezoelectric-diaphragm that drives the actuator, the exact dimensions and material properties are required as shown in Figure 2. Note the large uncertainties/tolerances associated with the dimensions of the device.

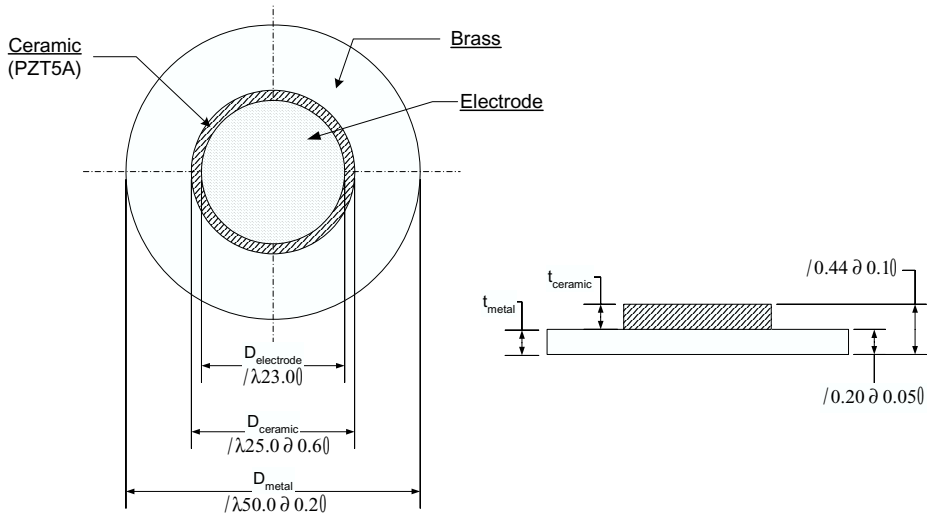

Figure 2: Schematic of the Murata type 7BB-50M-1 disk used in Case 1

Thus, in order to calculate the resonant frequency of the diaphragm we used the linear composite plate model developed by Prasad et al. [2]. Table 1 summarizes the input and output parameters of the piezoceramic driver.

Shim (Brass)	
Elastic Modulus (Pa)	$8.963\Delta10^{10}$
Poisson's Ratio	0.324
Density (kg/m^3)	8700
Thickness (mm)	0.15
Diameter (mm)	49
Piezoceramic (PZT-5A)	
Elastic Modulus (Pa)	$6.3\Delta10^{10}$
Poisson's Ratio	0.33
Density (kg/m^3)	7700
Thickness (mm)	0.31
Diameter (mm)	24.4
Rel. Dielectric Constant	1750
d_{31} (m/V)	$-1.75\Delta10^{-10}$
C_{EF} (F)	$1.12\ \Delta10^{-7}$
Voltage (V)	101.8
Calculated Lumped Parameters	
C_{aD} (s^2 m^4/kg)	$5.8\ \Delta10^{-11}$
M_{aD} (kg/m^4)	$2.062\Delta10^{3}$
λ_a (Pa/V)	2.2

Table 1: Piezoelectric-diaphragm specifications and parameters.

The measured amplitude of the phase-averaged vertical velocity component (provided in the workshop website) is used for comparison with the model. Three different measurement techniques were used, but the experimental data chosen for comparison here are the LDV measurements performed at ~0.1 mm above the center of the slot. The experimental value is referred to as $U_{CL}(\exp)$, while the model output is

denoted as U_{CL}. The input ac voltage used is 101.8 V, which is the mean of the fluctuating voltage given as input data (+100.97 V to -102.58 V).

The lumped element model predicts (with the only assumed empirical parameter being $'$ | 0.019, the diaphragm damping coefficient) the normalized response, $U_{CL}/U_{CL}/\exp()$, shown in Figure 3. In this case, the first resonant peak is dictated by the natural frequency of the diaphragm, and the second resonant peak is governed by the Helmholtz frequency of the cavity.

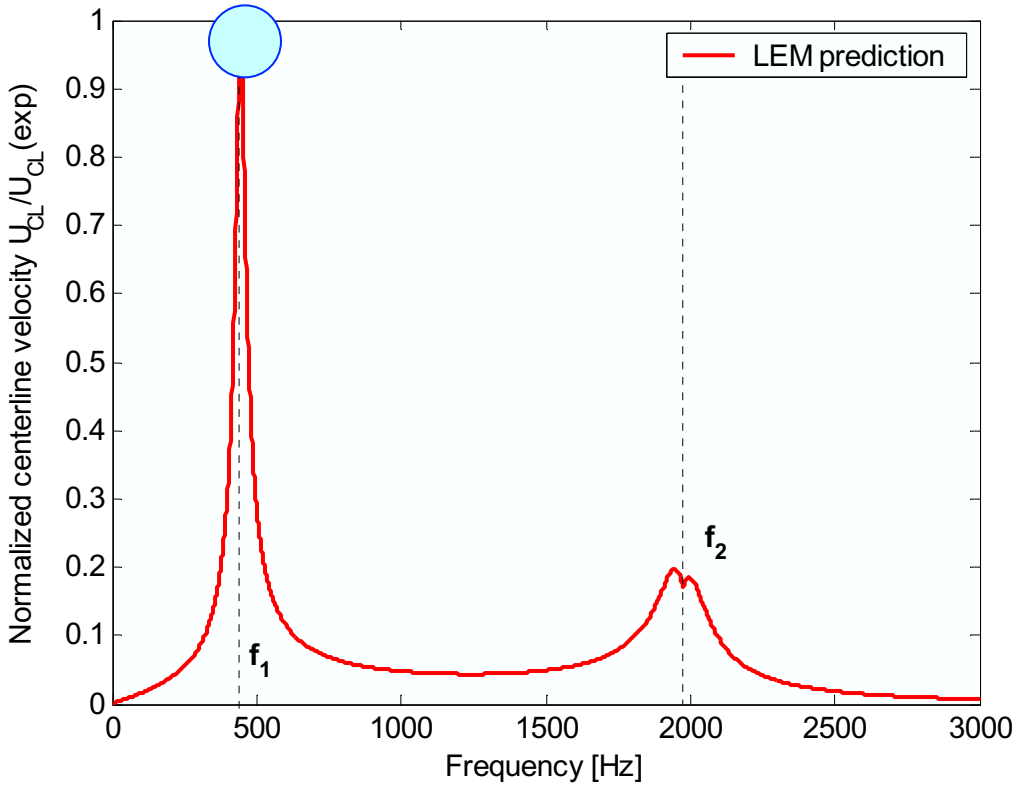

Figure 3: Frequency response of the synthetic jet actuator

The results are summarized in the following table:

	$U_{CL}/\exp()$ [m/s]	$U_{CL}/f_1()$ [m/s]
Exp. (LDV)	24.8	
LEM		24.7

Table 2: Comparison between experiment and model.

Clearly, the model results are in close agreement with the experimental measurements. However, the important point is not whether or not the model matches the experiment, but that the model gives a reasonable estimate (typically within ±20%) with minimal effort. The power of LEM is its simplicity and its usefulness as a design tool. LEM can be used to provide a reasonable estimate of the frequency response of the device as a function of the signal input, device geometry, and material and fluid properties.

Acknowledgements

The authors gratefully acknowledge support from AFOSR, monitored by Dr. Tom Beutner.

References

1. Gallas, Q., Holman, R., Nishida, T., Carroll, B., Sheplak, M., and Cattafesta, L., "Lumped Element Modeling of Piezoelectric-Driven Synthetic Jet Actuators," AIAA J., Vol. 41, No. 2, pp. 240-247, February 2003.
2. Prasad, S., Horowitz, S., Gallas, Q., Sankar, B., Cattafesta, L., and Sheplak, M., "Two-Port Electroacoustic Model of an Axisymmetric Piezoelectric Composite Plate," AIAA Paper 2002-1365, April 2002.

CASE 2: EXPERIMENTAL EVALUATION OF AN ISOLATED SYNTHETIC JET IN CROSSFLOW

Norman W. Schaeffler, Luther N. Jenkins, and Timothy E. Hepner

Flow Physics & Control Branch, NASA Langley Research Center, Hampton, VA 23681-2199

Introduction

The second case for this workshop builds upon the isolated synthetic jet of Case 1 by adding a crossflow, with no streamwise pressure gradient, for the developing jet to interact with. Formally, Case 2 examines the interaction of a single, isolated, synthetic jet and a fully turbulent zero-pressure gradient boundary layer. The resulting flow has many of the characteristics that need to be modeled with fidelity if the results of the calculations are to serve as the basis for research and design with active flow control devices. These include the turbulence in the boundary layer, the time-evolution of the large vortical structure emanating from the jet orifice and its subsequent interaction with and distortion by the boundary layer turbulence, and the effect of the suction cycle on the boundary layer flow.

In a synthetic jet, the flow through the orifice and out into the outer flowfield alternates between an exhaust and a suction cycle, driven by the contraction and expansion of a cavity internal to the actuator. In the present experiment, the volume changes in the internal cavity are accomplished by replacing one of the rigid walls of the cavity, the wall opposite the orifice exit, with a deformable wall. This flexible wall is driven by a bottom-mounted moveable piston. The piston is driven electro-mechanically. The synthetic jet issues into the external flow through a circular orifice. In the present experiment, this orifice has a diameter of 0.250 inches (6.35 mm). The flow is conceptually similar to that documented in Schaeffler [1].

To document the flow, several measurement techniques were utilized. The upstream boundary conditions (in-flow conditions), and several key phase-averaged velocity profiles were measured with a 3-component laser-Doppler velocimetry system. Phase-averaged velocity field measurements were made with both stereo digital particle image velocimetry and 2-D digital particle image velocimetry as the primary measurement system. Surface pressure measurements were made utilizing an electronically scanned pressure system.

Facility and Actuator Details

This research effort was conducted in the NASA Langley 15-inch Low Speed Wind Tunnel of the Flow Physics and Control Branch. This tunnel is a closed-return atmospheric facility dedicated to basic flow physics research efforts. The tunnel has a maximum speed of 115 ft/s and a turbulence intensity of less than 0.13%. The tunnel medium is air at sea level conditions. During this research effort, the tunnel was equipped with a suspended flat plate model that acts a splitter plate and facilitates the installation of the actuator within the plate model. The plate features an elliptical leading edge. Immediately downstream of the transition from the leading edge to the plate, there is a grit strip to trip the boundary layer of the plate and also grit strips at corresponding locations on the tunnel walls. The ceiling of this tunnel is adjustable at several locations down the length of the tunnel. The ceiling height was adjusted to create a zero pressure gradient over the plate starting from a station 24.8 inches (630 mm) downstream from the leading edge to a station 58.8 inches (1494 mm) downstream from the leading edge. The centerline of the jet was located 38.8 inches (986 mm) downstream of the leading edge. This results in the region of zero pressure gradient

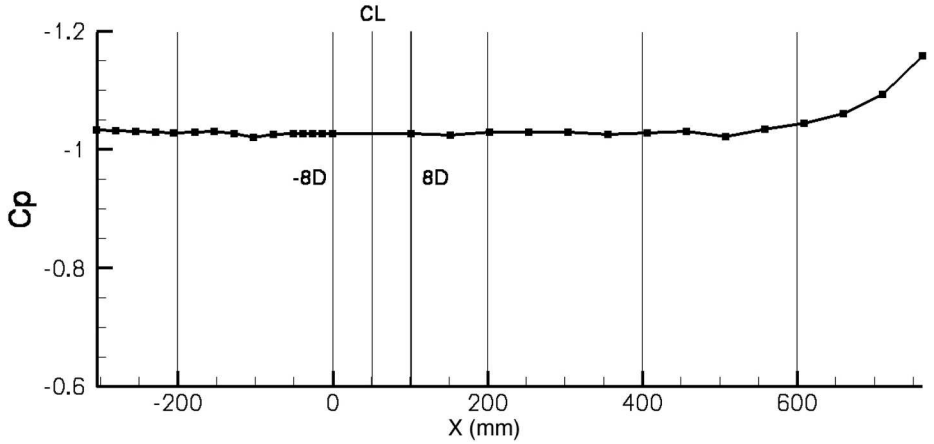

Figure 1: Pressure distribution down the centerline of the tunnel. X is measured in the streamwise direction, and X = 0.00 is the origin of the model coordinate system. The model coordinate system is shown schematically in Figure 4.

extending 56 jet diameters upstream of the jet centerline and 80 jet diameters downstream, as shown in Figure 1. These pressures were measured via a row of static pressure taps which are installed along the centerline of the tunnel with a total of 15 taps upstream of the jet exit and 15 taps downstream of the jet centerline, or exit. A set of spanwise pressure taps, 16 in total, were located 8 jet diameters upstream of the jet centerline and another set of spanwise taps, also 16 in total, were located 8 jet diameters downstream. All of these taps were connected via short lengths of flexible Tygon tubing to two ESP scanning pressure transducers, each with a full scale range of ± 10 inches of water. The ESP modules were mounted inside the plate model and the measured pressures are referenced to the static pressure of the tunnel, as observed by a Pitot-static tube upstream of the splitter plate. The modules were automatically calibrated at regular intervals during a given test day. The pressure data was used to calculate the freestream velocity over the plate and to verify that the pressure gradient over the plate, in the area of interest, was zero. Flow visualization conducted in this tunnel suggests that the flow is two-dimensional in the zero pressure gradient region of the plate, with the exception of the region close to the side walls [3].

The synthetic jet utilized in this research effort featured a circular orifice 0.25 inches (6.35 mm) in diameter. The throat of the orifice is smoothly tapered from a diameter of 0.60 inches (15.2 mm) on the inside cavity wall to the 0.25 inch diameter exit dimension. The actuator design is shown schematically in Figure 2. The active element of the actuator was the wall of the cavity opposite the exit of the jet, the bottom wall in Figure 2. This wall was displaced electro-mechanically by a sinusoidal voltage. To document the in situ performance of the actuator, the displacement of the actuator diaphragm was recorded, as was the cavity pressure and temperature. Two dynamic pressure transducers were installed in the interior of the cavity, one transducer referenced to the static pressure of the tunnel upstream of the splitter plate and the other transducer is an absolute transducer. A thermocouple was also located in the cavity. The diaphragm displacement and cavity pressure as a function of phase can be seen in Figure 3. The presentation of all of the subsequent velocity measurements utilize this same phase reference. The diaphragm displacement is relative to the nominal cavity depth when the tunnel is on condition. This value is 1.68 mm.

Boundary Conditions

In addition to the boundary conditions associated with the actuator, i.e., the diaphragm displacement, cavity pressure and temperature, the boundary conditions for this case additionally consist of the upstream, or in-

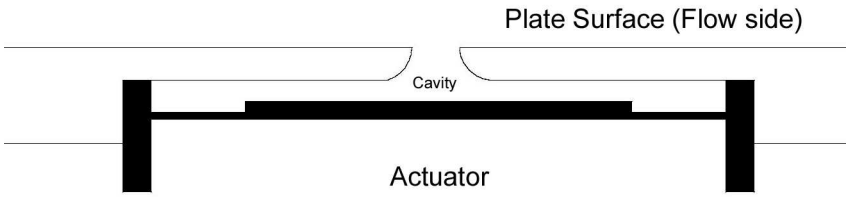

Figure 2: Schematic of the Synthetic Jet Actuator.

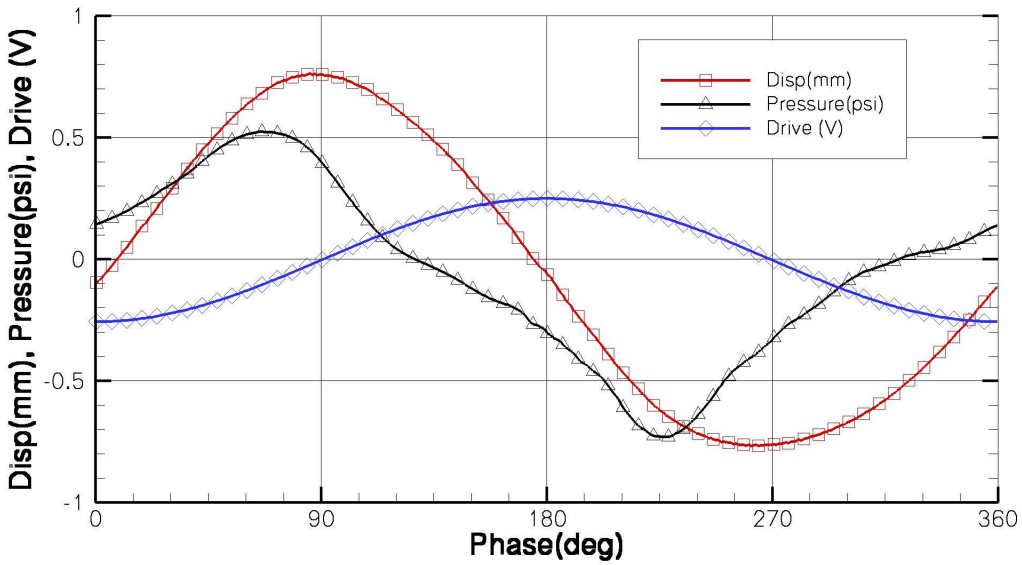

Figure 3: Diaphragm displacement, drive signal and cavity pressure as a function of phase for the Synthetic Jet Actuator.

flow, boundary condition, and the geometry of the model and the tunnel itself. The tunnel test condition was a Mach number in the test section over the plate of M = 0.10. The tunnel dimensions at the test section are 15.0 inches (381 mm) wide by 9.8 inch (249 mm) high (distance from the splitter plate to the top wall). The orifice diameter was 0.25±0.005 inches. The location of the jet orifice down the plate is specified in reference to the model coordinate system. The model coordinate system is shown schematically in Figure 4 and its origin was established where the first line of spanwise pressure taps intersects the line of centerline pressure taps. This location is 36.8 inches (935 mm) from the leading edge of the plate. In the model coordinate system, the centerline of the jet orifice is located at 2±0.020 inches (50.8±0.50 mm). Moving from the origin of the model coordinate system to the jet centerline in the streamwise direction defines the X coordinate axis, the Y coordinate axis is in the spanwise direction and the Z coordinate axis is in the vertical direction. The corresponding velocity components will be U, V, and W. From this point forward, distances in the streamwise, X, direction will be stated in millimeters or at times jet diameters from the jet centerline. The key locations are: x = 44.45 mm (-1D), x = 50.80 mm (0D, CL), x = 57.15 mm (1D), x = 63.50 mm (2D), x = 69.80 mm (3D), and x = 76.20 mm (4D).

While the atmospheric conditions varied on a daily basis, the conditions were never far from standard atmospheric conditions at sea level in a wind tunnel vented to the atmosphere, in a temperature-controlled room.

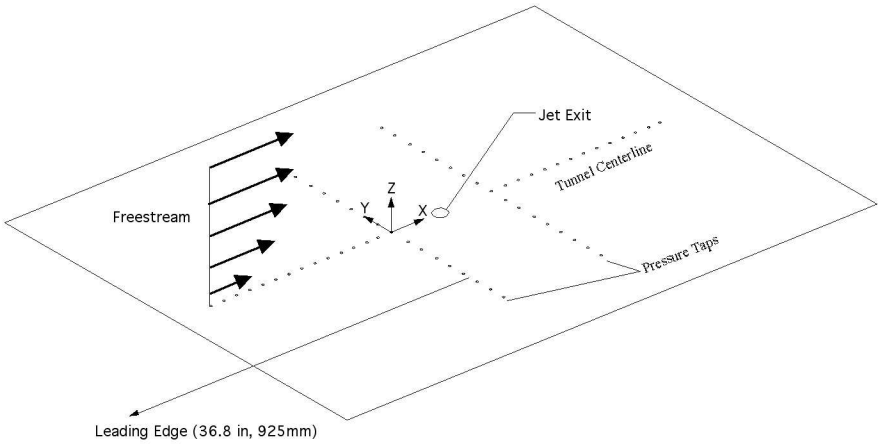

Figure 4: Schematic of the Model Coordinate System.

Freestream Mach Number	M_∞	0.10
Atmospheric Pressure	P_{atm}	101,325 Pa
Atmospheric Temperature	T_∞	23.9 °C (75 °F)
Density	ρ_∞	$1.185 kg/m^3$
Viscosity	μ_∞	$18.4x10^{-6} kg/ms$

Table 1: Atmospheric Conditions Observed for Case 2

These conditions are given in Table 1.

The upstream boundary conditions were measured at station x = 0.000 in the model coordinate system. A complete description of the state of the turbulent boundary layer was measured using the 3-component laser-Doppler velocimetry system to be described in the following section. All six components of the turbulent stress tensor were documented and presented as the upstream boundary condition. The velocity means and the turbulent stress components were compared to similar values available in the open literature, as shown for the mean profile of the freestream component of the velocity, U, in Figure 5.

Instrumentation and Data Acquisition

The velocity measurements to support Case 2 were carried out using a 3-component laser-Doppler velocimetry (LDV) system, a stereo (3D) digital particle image velocimetry (SDPIV) system, and a 2D digital particle image velocimetry (2D-PIV) system. The two PIV systems were the primary technique for measuring the velocity field. The LDV system was an orthogonal, crossed-fringe, fiber-optic probe configuration, with the probes mounted 90° from one another. The 514.5, 496.5, and 476.5 nanometer wavelengths from an Argon-Ion laser were used to measure the spanwise (V), vertical (W), and streamwise (U) velocity components, respectively within the tunnel. Bragg cells were utilized to provide directional measurement capability in all three velocity components. Both fiber optics probes used 750-mm focal length lenses, which along with an input beam diameter of 3 to 4mm, generated a sample volume calculated to be approximately 100 μm in diameter and spherical in shape. The optical setup of the LDV system can be seen in Figure 6. All velocity measurements were made in coincidence mode. Coincidence mode requires that a validated velocity signal be made independently in each of the three components within a very short time window, guaranteeing that

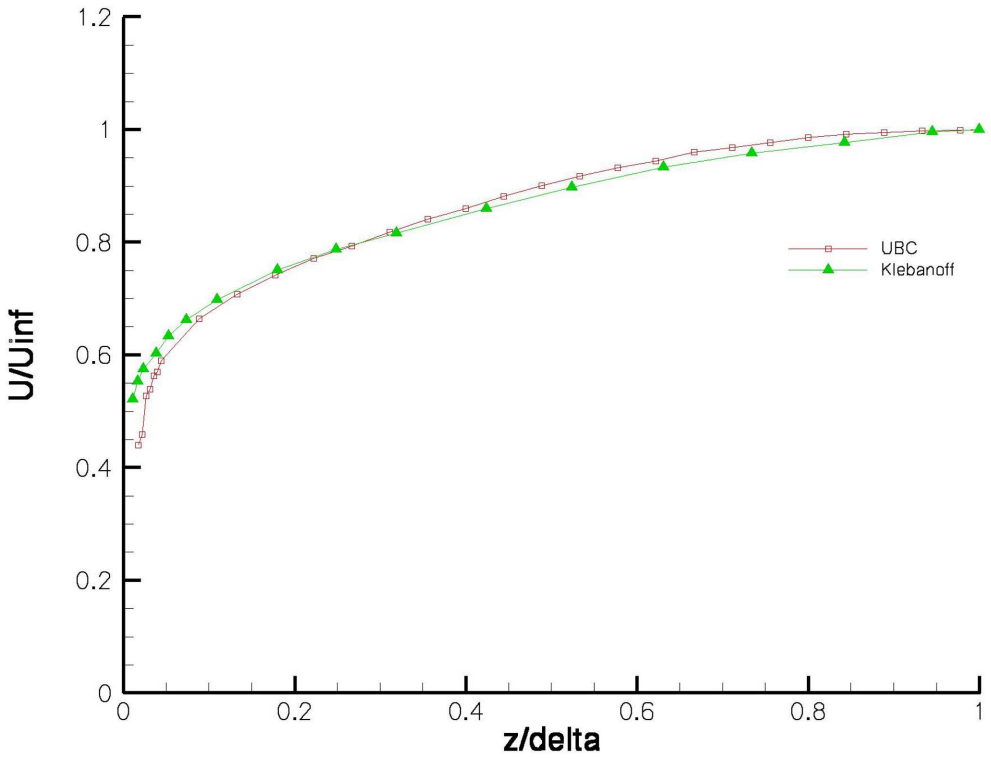

Figure 5: Upstream Boundary Condition on U compared to the data of Klebanoff[4]

the velocity signals come from a single particle traversing the measuring volume. The use of coincidence mode is required to make full turbulence measurements with an LDV system. The use of coincidence in the present research effort allows each of the six components of the turbulent stress tensor to be measured.

Additionally, the actuator drive and sync signal were acquired with each trigger and stored if the point was validated as being in coincidence. Consideration of the actuator drive and sync signal allows the LDV data, which is acquired at random intervals, to be reconstructed as a function of phase. The fiber optics probes were mounted on a X95 rail frame traversing system. The traversing system utilized several motorized slides that provided 1 meter of travel in each of the three axes, with 1 μm resolution in each direction. For the LDV portion of the experiment, the flow was seeded with mono-disperse, 0.86 μm polystyrene latex (PSL) micro-spheres. The seed particles were suspended in 100-proof alcohol and atomized by a six-jet atomizer. The atomized particles were then introduced into the settling chamber of the tunnel. The particles were fabricated at NASA Langley using the technique described by Nichols[2].

In processing the data from the LDV system, we wish to relate the velocities measured to a particular phase of the actuator. The LDV system acquires, along with the coincident velocity data, data for the drive signal of the actuator and a sync signal. Analysis of these values allows for the reconstruction of the phase angle at the time of acquisition and was used to phase average the LDV data record at every point. Once the phase angle of each piece of LDV data is calculated, the data can be grouped into bins according to phase angle. Each bin represents data with a phase angle in a certain range. For the data in Case 2, this range was 10°. The bin was then averaged to yield the phase-average at that point. The uncertainty in the phase-averaged LDV mean data is estimated to be $\pm 0.5\%$. Once all the phase-averaging was accomplished, each of the phase-averaged series was averaged as a time series to calculate the long-time average at each point. The long-time average velocity profiles derived from the LDV data are shown in Figure 7.

The timing control, image acquisition, data management and post-processing of both the stereo PIV and the 2-D PIV data was handled by a commercial system. The light source utilized was a pulsed, frequency-

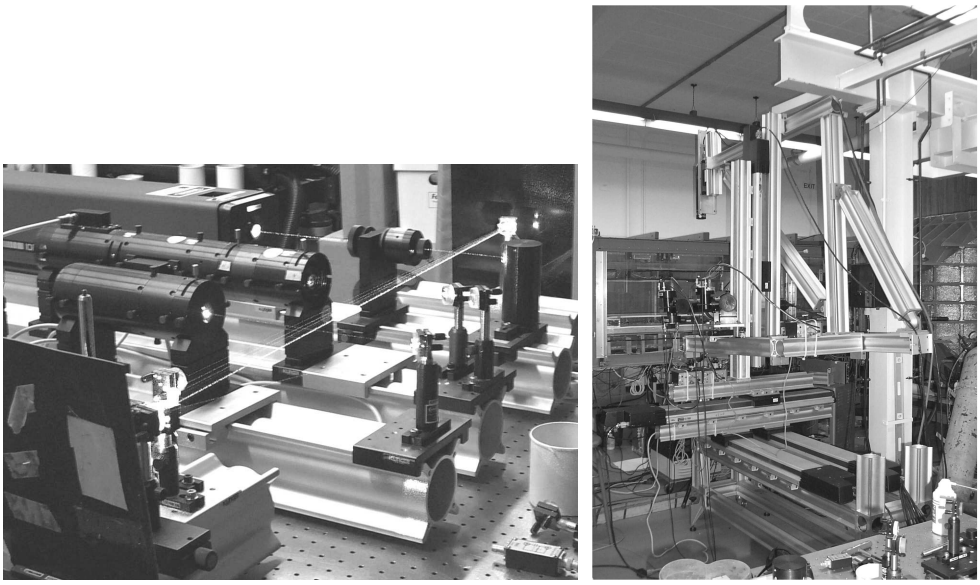

(a) Laser and Optical Configuration

(b) Fiber Optic Bundles and Traversing System

Figure 6: The Laser-Doppler Velocimetry Setup.

doubled 300 mJ Nd-YAG laser operating at 10 Hz. For the PIV portion of the experiment, the flow within the tunnel was seeded with atomized mineral oil with a typical particle size of 2 microns. The seed was injected into the flow in the tunnel settling chamber. Standard sheet-forming optics were utilized and the cameras were positioned on opposite sides of the tunnel for the SDPIV data. Also for the SDPIV, the camera mounts allow for the required tilting of the lens, relative to the camera body, in order to satisfy the Scheimpflug condition. The light sheet orientation for the SDPIV data was in the spanwise direction and in the streamwise direction for the 2D-PIV data. The position of the sheet in the spanwise direction was controlled by a prism mounted on the same traversing system utilized by the LDV system. The light sheet thickness was typically 1.5 mm thick. The resolution of each camera was 1008 x 1018 pixels and the typical field of view was 40 mm x 40 mm for the SDPIV and 18 mm x 18 mm for the 2D-PIV.

The image acquisition and lasers for both PIV systems were synchronized with the drive signal of the actuator so that images could be acquired at a specific time delay after the beginning of a cycle of the actuator drive signal. A specific delay for the laser pulsing and image acquisition corresponds to a specific phase of the actuator drive cycle. The same sync signal that the LDV system acquired was used as the trigger for the PIV signal. Within the PIV software, the timing delay was varied in order to acquire data at 36 specific phases of the synthetic jet actuator drive signal, equally spaced over both the exhaust and suction cycles. The flowfield over the entire drive signal was recorded as 10,800 instantaneous velocity fields, 300 velocity field measurements at each of 36 specific delays, which results in the measurement of the velocity field every 10 degrees of phase. The 300 image pairs were acquired over a period of 3 minutes and were processed using a standard PIV cross-correlation data reduction technique and then averaged to give the phase-averaged, or ensemble-averaged, velocity field. The uncertainty in the phase-averaged 2D-PIV mean data is estimated to be $\pm 1.3\%$. These phase-averaged velocity fields were be ordered in time allowing the evolution of the jet-induced velocity field, and its interaction with the crossflow, to be studied. The long-time average of the velocity field was calculated by averaging, through one complete cycle, the individual phase-averaged velocity fields, as shown in Figure 8 for data derived from the 2-D PIV system.

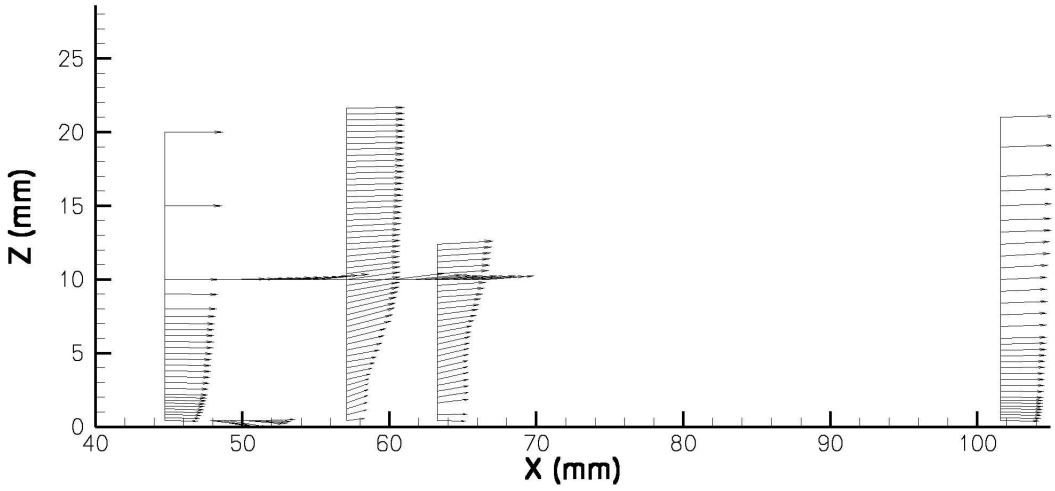

Figure 7: Long-Time Average Velocity Profiles from the LDV data.

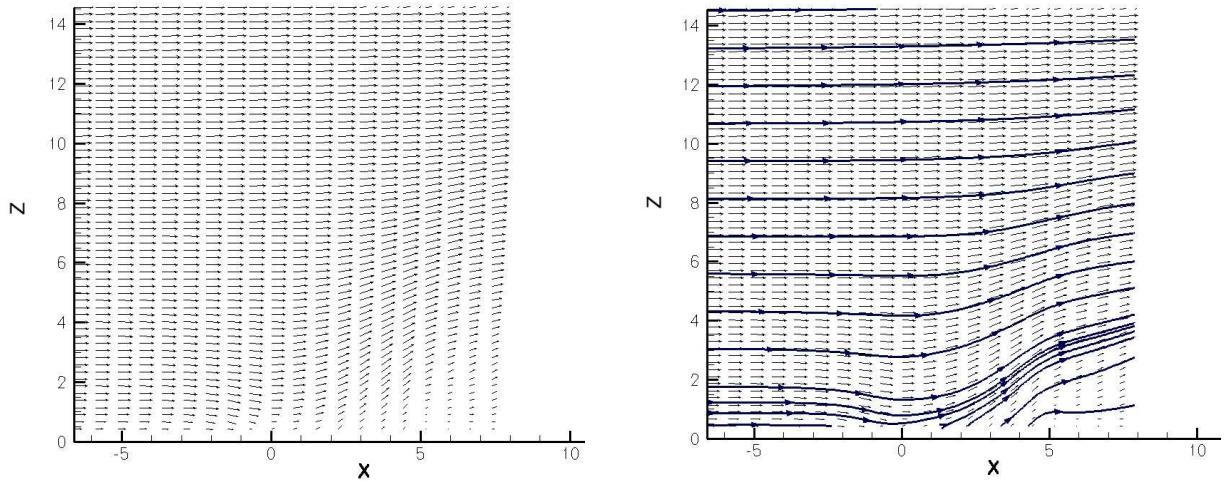

(a) Velocity Vectors

(b) Velocity Vectors and Streamlines

Figure 8: Long-time average Velocity Field via 2-D PIV. In these figures, x = 0 corresponds to X = 50.325 mm in the model coordinate system.

References

[1] Schaeffler, N. W. "The Interaction of a Synthetic Jet and a Turbulent Boundary Layer," AIAA Paper No. 2003-0643, 2003.

[2] Nichols, C. E., "Preparation of Polystrene Microspheres for Laser Velocimetry in Wind Tunnels," NASA TM-89163, 1987.

[3] Jenkins, L., Althoff Gorton, S., and Anders, A., "Flow Control Device Evaluation for an Internal Flow with an Adverse Pressure Gradient," AIAA Paper No. 2002-0266, 2002.

[4] Klebanoff, P. S., “Characteristics of Turbulence in a Boundary Layer with Zero Pressure Gradient,” NACA TR-1247, 1953.